Supplementary Materials for

Identification of Non-Metal Single Atomic Phosphorus Active Sites for CO_2 Reduction Reaction

MATERIALS AND METHODS

Chemicals

Melamine (99 %, molar mass: 126.12 g/mol), L-alanine (98 %, molar mass: 89.09 g/mol), hydrochloric acid (37 %), $KHCO_3$ (99.7 %) and Nafion® 117 solution (~5 % in a mixture of low aliphatic alcohols) were purchased from Sigma-Aldrich and used directly without further purification. Glyphosate (98 %, molar mass: 169.07 g/mol) was purchased from MAYA-R and used directly without further purification. Deionized water from Millipore Q water purification system was used to make the solutions.

Synthesis of P-SAC-NG and NG

In a typical synthesis of P-SAC-NG, 9 g of melamine and 1.52 g of glyphosate were homogeneously mixed by ball milling for 1 h in a ZrO_2 mortar. Then, 15 mL mixed solution of hydrochloric acid and ethanol (volume ratio 1 : 5) was added and the slurry was put in a mortar. The mixture was milled in a fume hood until all ethanol was evaporated. The resultant solid was dried in an oven at 60 ^oC overnight and ball milled again for 10 min. Subsequently, the fine powder mixture was undergone a two-stage pyrolysis and carbonization process (first stage: from 25 to 600 °C at a ramping rate of 3 °C/min, maintain at 600 °C for 2 h; second stage: from 600 to 900

°C at a ramping rate of 2 °C/min, maintain at 900 °C for 90 min) in a tubular furnace (Carbolite, UK) in argon atmosphere. After cooling down to room temperature under argon atmosphere, the final product was collected for subsequent characterization. The control sample (nitrogen doped graphene, NG) was synthesized by the same procedure just replacing glyphosate with the same mole amount of L-alanine.

Characterizations

Crystal structure and morphology of the catalysts were examined by X-ray diffraction (XRD, Bruker AXS D8 Advance) with Cu K_α radiation (λ = 1.5406 Å), field-emission scanning electron microscopy (FESEM, JEOL JSM-6700F), transmission electron microscopy (TEM, JEOL JEM-2100F) and atomic force microscopy (Nanoman, Veeco, Santa Barbara, CA) using the tapping mode. Chemical states and composition of the samples were analyzed by X-ray photoelectron spectroscopy (XPS) on an ESCALAB 250 photoelectron spectrometer (Thermo Fisher Scientific) using a monochromatic Al K_α X-ray beam (1486.6 eV). All binding energies were referenced to the C 1s peak (284.6 eV). Specific surface area was measured based on the BET method on Micromeritics 3Flex BET (Micromeritics Instrument Corporation, USA) at liquid-nitrogen temperature. Sub-ångström-resolution high-angle annular dark-field scanning transmission electron microscopy (HAADF-STEM) characterization was conducted on a JEOL JEMARM200F STEM/TEM with a guaranteed resolution of 0.08 nm. Solid-state nuclear magnetic resonance (NMR) spectroscopy measurements were conducted on Bruker Avance III HD 800 MHz spectrometer. The chemical shifts are referenced to external 85% H_3PO_4. The content of elements in the sample was quantified by inductively coupled plasma-mass spectrometry (ICP-MS, PerkinElmer Elan DRC-e).

Electrochemical measurements

All electrochemical measurements were carried out at ambient temperature and pressure on a rotating disc electrode system (Pine Inc.) with a CHI 760e potentiostat. A three-electrode cell configuration was employed with a working electrode of glassy carbon rotating disc electrode (RDE) of 5 mm diameter, a counter electrode of graphite rod (5 mm diameter), and a saturated calomel reference electrode (SCE). To prepare the catalyst ink, 5 mg of catalyst and 25 μL of 5 % Nafion® 117 solution (DuPont) as conducting binder were introduced into 975 μL of water-isopropanol solution with equal volume of water and isopropanol and sonicated for 3 h. An aliquot of 6 μL of the catalyst ink was applied onto a glassy carbon RDE and allowed to dry in air, giving a catalyst loading of 0.15 mg cm^{-2}. A CO_2-saturated electrolyte was prepared by purging CO_2 (99.99 %) into 0.5 M $KHCO_3$ aqueous solution for 20 min, and a flow (100 cc/min) of CO_2 was maintained over the electrolyte throughout the electrochemical measurements. For comparison, CV measurements were also performed in an Ar (99.99 %)-saturated electrolyte. All potentials were calculated with respect to the reversible hydrogen electrode (RHE) scale according to the Nernst equation ($E_{RHE} = E_{SCE} + 0.05916 \times pH + 0.241$ V, at 25 °C). All pH was determined by a pH meter (S220 SevenCompact™ pH/Ion). The pH of CO_2-saturated and Ar-saturated 0.5 M $KHCO_3$ was 7.3 and 8.4, respectively. The linear sweep voltammograms (LSVs) were collected at a scan rate of 5 mV s^{-1}. The Tafel slope was calculated based on the Tafel equation ($\eta = b*log(j_{CO}/j_o)$), where η is the overpotential, b is the Tafel slope, j_{CO} is the current density for CO formation, and j_o is the exchange current density. All LSV data were corrected for the Ohmic drop, the solution resistance was determined by electrochemical impedance spectroscopy (EIS) measurement. All current densities were normalized to the geometric area of the electrode.

H-type electrochemical cell for CO_2 reduction

The products and Faradaic efficiency of CO_2 reduction were measured using chronoamperometry at each fixed potential in an H-type electrochemical cell separated by a Nafion®117 membrane. The area of the working electrode is fixed at 1 cm^2. To prepare the working electrode, the catalyst ink (10 mg ml^{-1}) was brush-painted directly onto a dry carbon fiber paper (CFP) (AvCarb P75T) at 50 ^oC, giving a catalyst loading of 0.5 mg cm^{-2}. The gaseous products (i.e., H_2, CO and CH_4) were quantified by a gas chromatography (GC, Agilent 7890) equipped with a flame ionization detector (FID) for CO and CH_4 and a thermal conductivity detector (TCD) for H_2 quantification. Ultra-pure helium (He, 99.9999 %) was used as the carrier gas. The flow rate of CO_2 was controlled at 8 cc min^{-1} at the inlet of electrochemical cell by a standard series mass flow controller (Alicat Scientific mc-50 sccm) and measured by a flow meter (Thermo Scientific GFM Pro) at the exit of the electrochemical cell. GC was calibrated using standard gas mixtures (Singapore Oxygen Air Liquide Pte Ltd) under standard conditions (1 atm and 298 K). To confirm the CO_2RR, isotopic $^{13}CO_2$ as the feedstock for the electrochemical reduction was conducted at room temperature in 0.2 M Na_2SO_4 aqueous solution with Ar as the carrying gas.

Faradaic efficiency (FE) quantification

Based on the definition of Faradaic efficiency:

$$FE_i = \frac{Q_i}{Q_{total}} \qquad (1), \qquad where\ i\ represents\ species\ CO, H_2\ or\ CH_4.$$

Q_i and Q_{total} can be obtained from the following equations:

$$Q_i = Z_i * F * N_i \qquad (2)$$

$$Q_{total} = I * t \qquad (3)$$

Based on the GC data and ideal gas law:

$$N_i = N_{total} * V_i \quad (4)$$

$$N_{total} = \frac{P_o * V_o}{R * T_o} \quad (5)$$

$$V_o = G * t \quad (6)$$

where G is the volumetric flow rate;

So, equation (1) can be written as: $FE = \frac{z_i * v_i * G * F * P_o}{I * R * T_o * 60000}$;

where N_i: mole of product i in the GC sampling loop;

N_{total}: mole of all gases in the GC sampling loop;

V_o: volume of the GC sampling loop;

t: time for gas to fill the GC sampling loop;

I: the average current in a period (t) of electrocatalysis: $I = \frac{\int_0^t I(t)dt}{t}$;

V_i: the volume ratio of product i in the GC sampling loop;

Z_i: number of electrons required to produce an i molecule, which is 2, 2 and 8 for CO, H_2 and CH_4, respectively;

F: Faradaic constant (96485.33289 C mol^{-1});

P_0: atmospheric pressure 1.013×10^5 Pa;

T: reaction temperature of 298 K;

R: ideal gas constant, 8.314 J·mol·K^{-1}.

X-ray absorption near edge structure (XANES)

Electronic structure was probed by the XAS measurements, which were performed at the National Synchrotron Radiation Research Centre (NSRRC, Hsinchu, Taiwan). The 1.5 GeV electrons were injected into storage ring with a beam current of 360 mA. The K-edge X-ray absorption spectra of C, N and O were measured in total electron yield mode at room temperature using BL20A. The P-SAC-NG and NG were supported on microporous support layer (nickel foam) under 20 MPa pressure. Before XANES measurements, the samples were reacted in a CO_2-saturated 0.5 M $KHCO_3$ aqueous solution for 30 min at -0.8 V vs. RHE. After CO_2RR, the samples were soaked in deionized water and dried in vacuum, and then subjected to an ultrahigh vacuum chamber (1×10^{-9} torr) for the total electron yield X-ray absorption spectra (TEY-XAS) collection. The data were collected at the 6 m high-energy spherical grating monochromator (HSGM) beamline with 1×1 mm^2 opening slits, corresponding to ~0.08 eV energy resolution. Simultaneously, the incident beam intensity from a gold grid located upstream in the X-ray path was recorded, and the spectra were normalized using the incident beam intensity. P K-edge XANES spectra were measured on BL16A in total fluorescence yield (TFY). A Si (111) double-crystal monochromator (DCM) was used, and the energy resolution was about 0.15 eV for the near-edge structure. Incident beam intensity was measured with a helium filled ion chamber. Different standards (C K-edge (SiC), N K-edge (BN), O K-edge (NiO), P K-edge (Zr foil)) were used for energy calibration.

In-situ **attenuated total reflectance (ATR) surface-enhanced infrared absorption spectroscopy (ATR-SEIRAS) measurements.**

The attenuated total reflectance surface enhanced infrared absorption spectroscopy (ATR-SEIRAS) experiments were performed on a Nicolet iS50 FTIR spectrometer equipped with a MCT detector cooled with liquid nitrogen and PIKE VeeMAX III variable angle ATR sampling

accessory. The catalyst ink was drop-casted on an Au-coated Si prism surface, which was prepared as reported by Cai and coworkers (*1, 2*). The other conditions were kept the same as the CO_2 electroreduction performance test. The IR spectra were collected at each constant potential from -0.2 V to -0.9 V vs. RHE.

Real-time X-ray and ultraviolet photoelectron spectroscopy (XPS and UPS) investigations

The real-time XPS experiments were performed in a lab-based Specs Phoibos 150 near ambient pressure (NAP) system with a conventional Al/Mg twin X-ray source and helium-I source. The pass energy was set at 20 eV, and the full width at half maximum (FWHM) for C 1s was ~1.5 eV. All binding energies were referenced to the C 1s peak (284.6 eV). The UPS measurements were carried out in the same NAP-XPS system. A 300-μm nozzle was used and the sample was illuminated directly by the helium-I source ($h\nu$ = 21.2 eV) using a VUV lamp (VG Microtech 232). The sample was earthed (no bias voltage) with an emission angle of ~40˚. The pass energy of the analyzer was set at 2 eV. The P-SAC-NG and NG catalysts were dispersed in deionized water, and then drop-casted on pre-cleaned graphite sheet. UPS and XPS spectra were first collected from clean catalysts, which were thermally treated at 450 ^{o}C for 30 min in vacuum to remove adsorbed gas and water molecules. Subsequently, the catalysts were exposed to high purity CO_2 gas (99.999 %, CryoExpress Singapore) in the preparation chamber at 1 atm for 20 min.

Theoretical methods and computational details

All theoretical calculations were performed using spin-polarized density functional theory (DFT) with the Vienna ab initio simulation package (VASP) (*3-5*). The projector augmented wave (PAW) (*6*) method was used to define the interactions between the ion cores and valence electrons and the generalized gradient approximation (GGA) method with Perdew−Burke−Ernzerhof (PBE) (*7*) exchange-correlation functional was used as implemented in VASP. The plane wave kinetic

energy cutoff of 500 eV was used. The Brillouin zone in the reciprocal space was sampled at the gamma point. All ions were allowed to relax until the maximum force became less than 0.01 eV/Å. Phosphorus atom was doped on the armchair edge of graphene nanoribbons, at both edges of which the unsaturated dangling C-C bonds were terminated with hydrogen atoms. In the supercell arrangement, we preserved a sufficiently large vacuum gap of 12 Å along the y-axis and 15 Å along the z-axis to avoid unrealistic inter-cell interactions.

The adsorption energy (E_{ads}) of the reaction intermediates was calculated according to the equation, $E_{ads} = E_{adsorbate/P\text{-}SAC} - (E_{adsorbate} + E_{P\text{-}SAC\text{-}NG})$, where $E_{adsorbate/P\text{-}SAC\text{-}NG}$, $E_{adsorbate}$ and $E_{P\text{-}SAC\text{-}NG}$ represent the energies of species adsorbed on P-SAC-NG, the free adsorbate, and the P-SAC-NG catalyst, respectively. The Gibbs free energy was calculated as $G = E_{DFT} + E_{ZPE} - TS$, where E_{DFT}, E_{ZPE} and S denote the electronic energy obtained from DFT calculation, zero point energy, entropy at $T = 298.15$ K, respectively. The entropy of gaseous molecule (H_2, CO_2, CO, H_2O) was taken from the NIST database (*8*). The free energy at an applied electrode potential U was calculated as $G_U = G - neU$. The free energies of the proton and electron transfer steps in the reaction were calculated based on the computational hydrogen electrode (CHE) model as proposed by Nørskov and co-workers (*9*), where the free energy of proton (G_{H+}) equals to that of the hydrogen atom in gaseous H_2 ($1/2G_{H2}$).

Generally, the two-electron CO_2RR ($CO_2 + 2H^+ + 2e^- \rightarrow CO + H_2O$, $E^0 = -0.11$ eV) proceeds via the following elementary steps (*10, 11*):

$$* + CO_2 + H^+ + e^- \rightarrow *COOH \quad (1)$$

$$*COOH + H^+ + e^- \rightarrow *CO + H_2O \quad (2)$$

$$*CO \rightarrow * + CO \quad (3)$$

where * denotes the active site.

Orbital interactions in the cluster model were studied using the Amsterdam Density Functional (ADF 2016.106) program (*12, 13*), together with the TZ2P Slater basis sets. Frozen core approximations were applied to the inner shells [$1s^2$] for C, N atoms and [$1s^2$-$2p^6$] for P atom. The scalar relativistic effects were taken into account by adopting the zero-order-regular approximation (ZORA) (*14*). Electron charge transfer was calculated with a grid-based Bader analysis (*15, 16*).

Supplementary Figures:

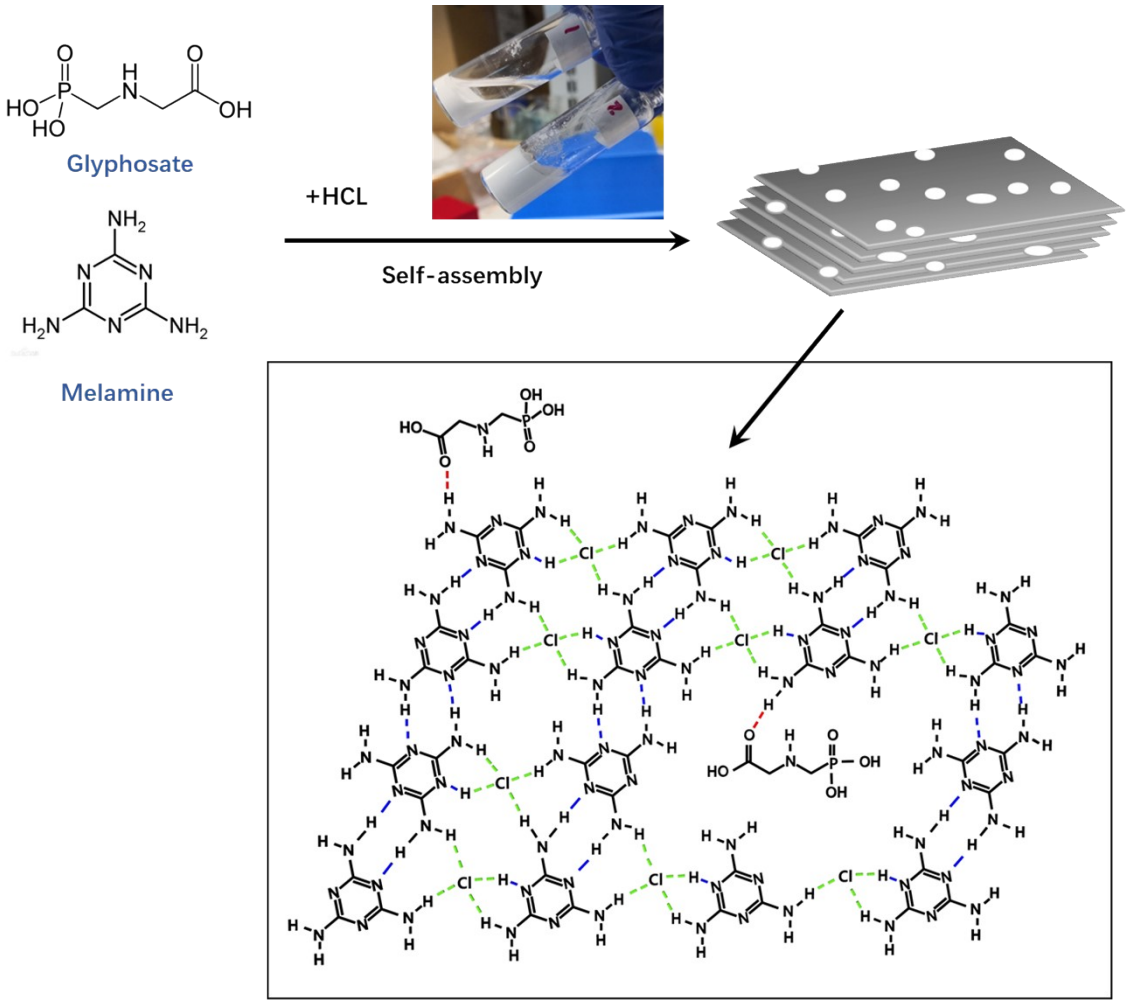

Figure S1. Schematic illustration showing the preparation process for the P-SAC-NG. Digital picture shows 2 g of ball-milled mixture of melamine and glyphosate blended with 3 mL of ethanol (1) and ethanol + HCl (5:1) solution (2). The bottom figure schematically illustrates the formation of supramolecular by self-assembling melamine and glyphosate via hydrogen bond and Cl^- ion (*17*).

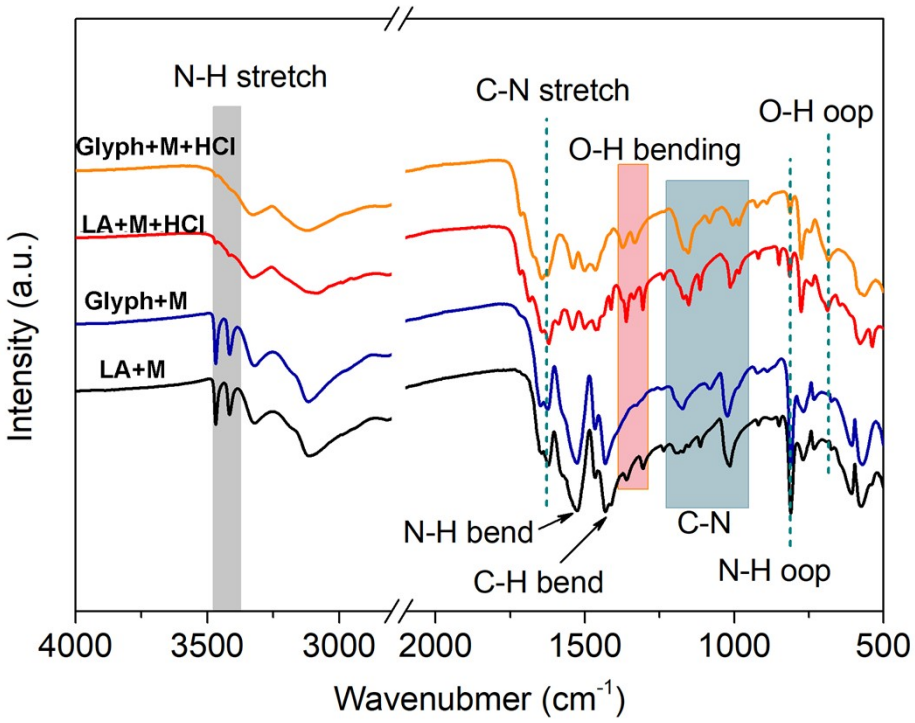

Figure S2. FTIR spectra of mixture precursors after ball milling and HCl assisted self-assembly. M refers to melamine, Glyph refers to glyphosate, and LA refers to L-alanine. The disappearance of the stretching, deformation bands and vibration of out of plane (oop) of the amine groups (ν_{NH2}) at 3464–3410 cm^{-1}, 1522 cm^{-1} and 810 cm^{-1}, similar to previous observations (*17, 18*), show the interaction between melamine and the halogen acids.

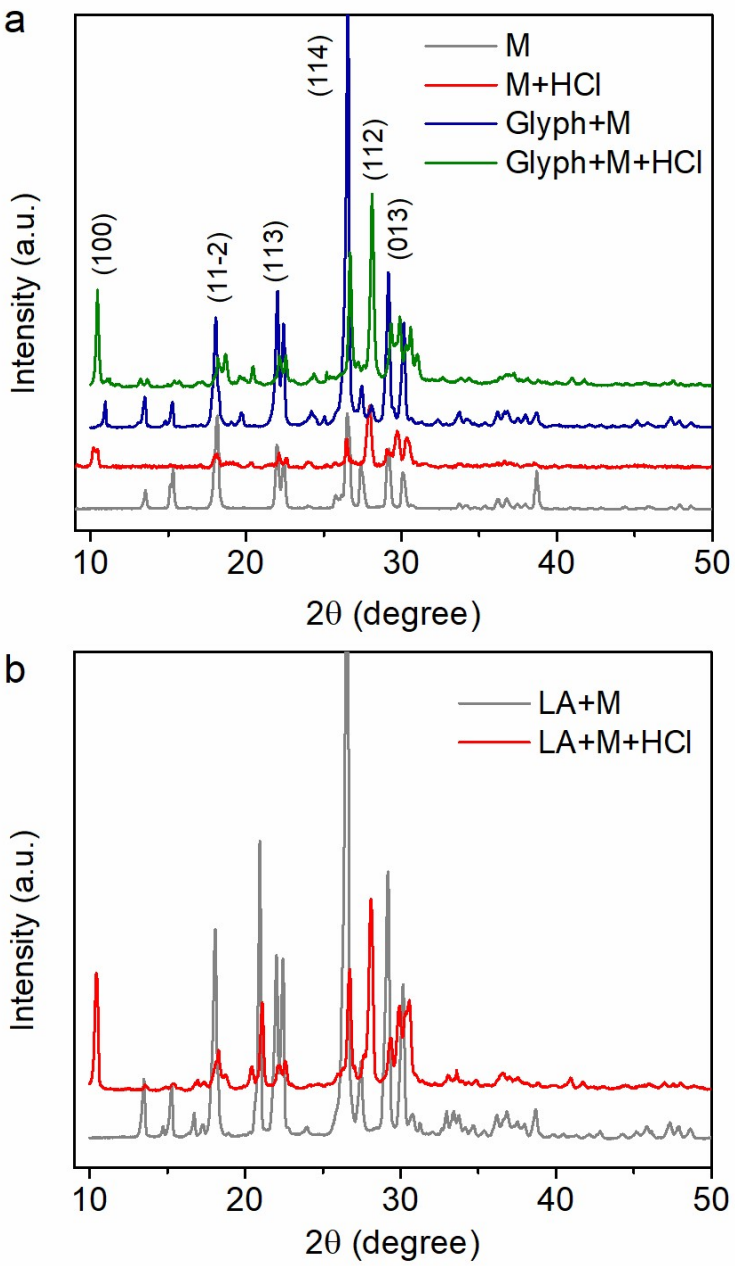

Figure S3. X-ray diffraction patterns of ball milled precursor mixture and the precursor after HCl assisted self-assembly (a) Melamine (M), Melamine + Glyphosate (Glyph), (b) Melamine + L-alanine (LA). Note: as shown in (a) and (b), the two new peaks emerged at 10.5° and 20.2° for both assemblies of M + LA and M + Glyph assisted by HCl, correspond to the periodic alignment of melamine units along the (100) and (112) direction with π-π interaction, owing to the interaction of Cl^- ion with melamine units (*18*).

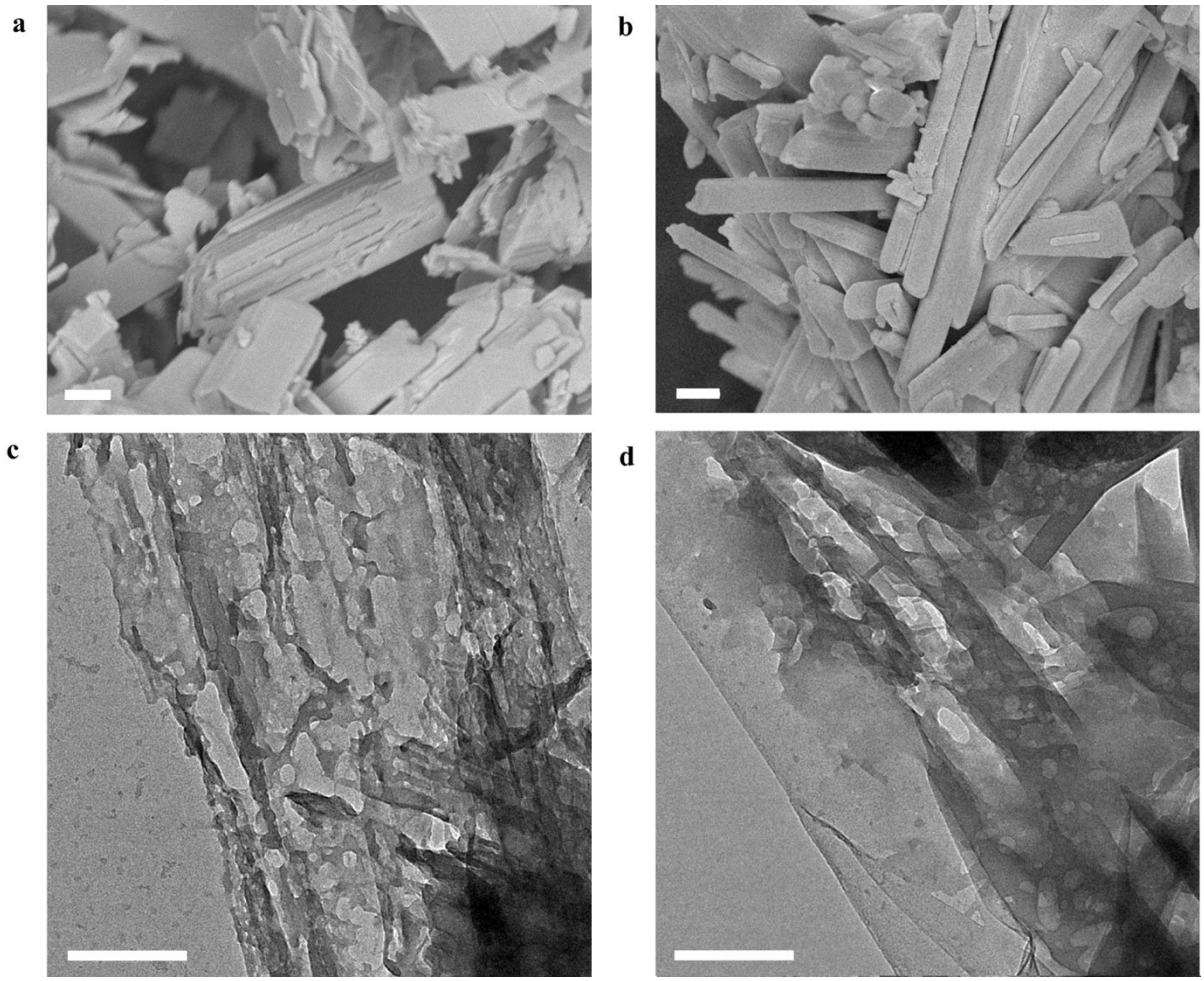

Figure S4. SEM (a, b) and TEM (c, d) images of the precursor after HCl assisted self-assembly. (a, d) Melamine and glyphosate, (c, d) Melamine and L-alanine. Scale bars are 1 um and 100 nm in (a, b) and (c, d), respectively. Note: SEM and TEM images show similar plate-like aggregates for M + Glyph and M + LA assemblies; the major distinction between these two assemblies in morphology is that M + Glyph assembly is more porous.

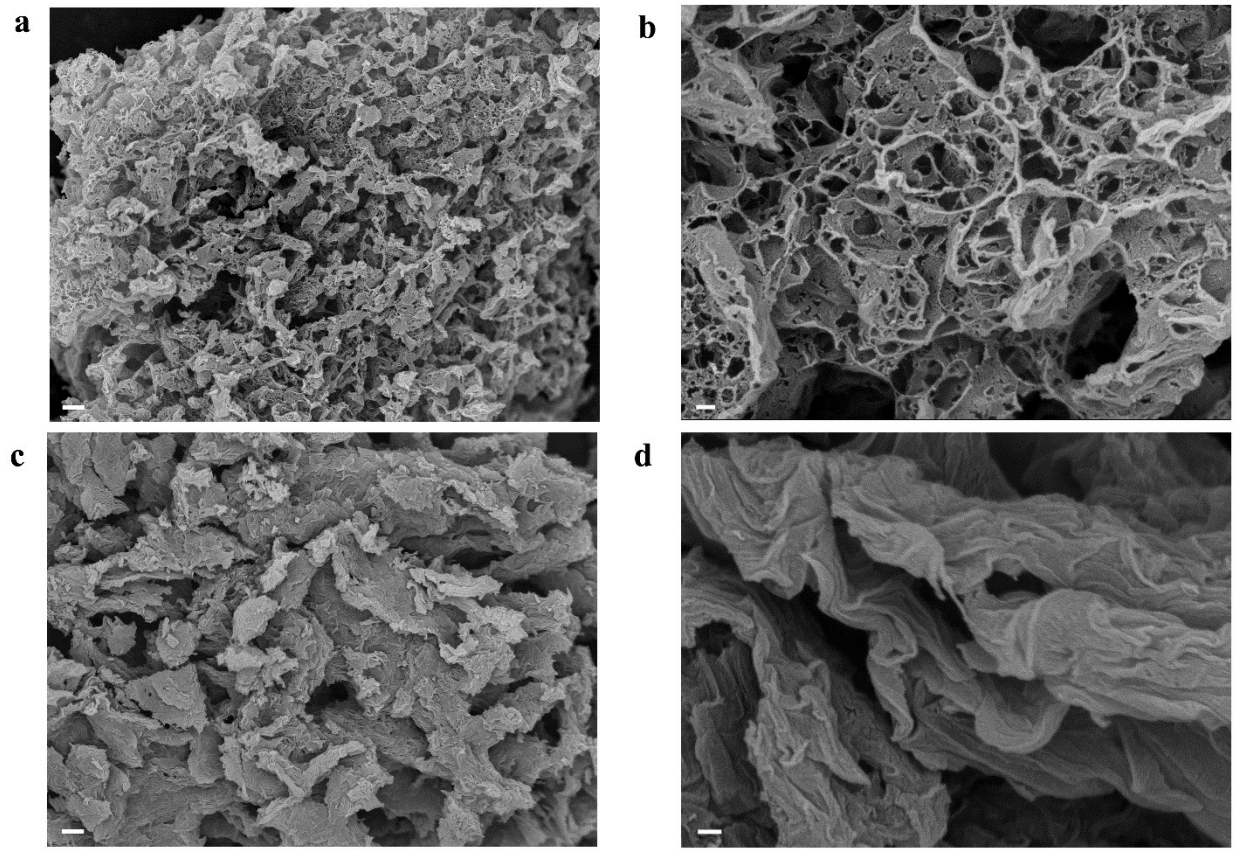

Figure S5. SEM images of P-SAC-NG (a, b) and NG (c, d). Scale bars are 1 um and 100 nm in (a, c) and (b, d), respectively.

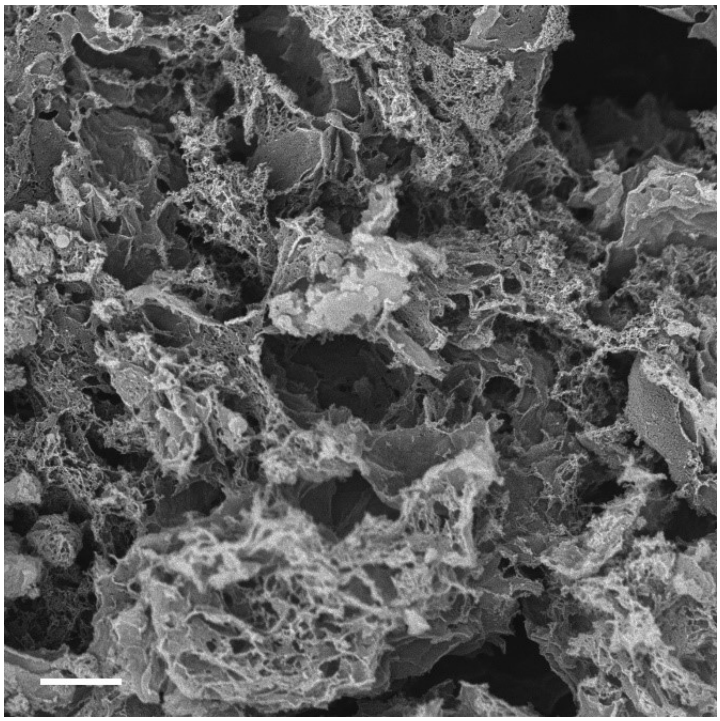

Figure S6. SEM image of P-SAC-NG synthesized from the precursor without undergoing HCl assisted self-assembly. Scale bar is 100 nm.

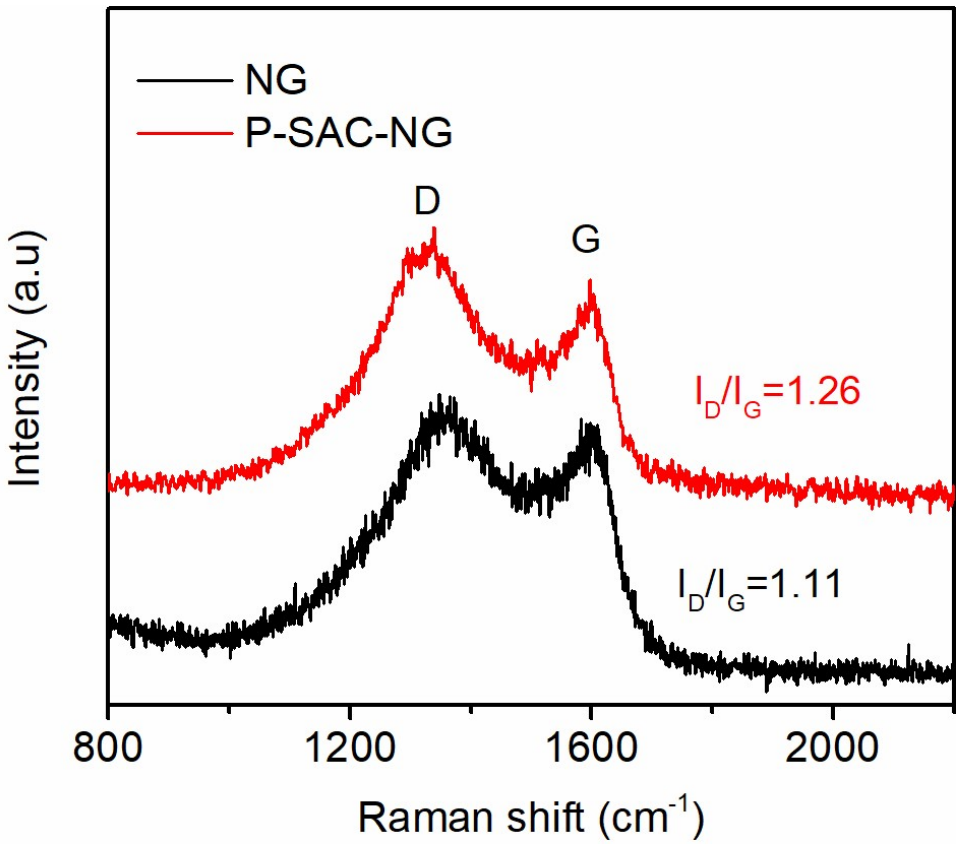

Figure S7. Raman spectrum of NG and P-SAC-NG.

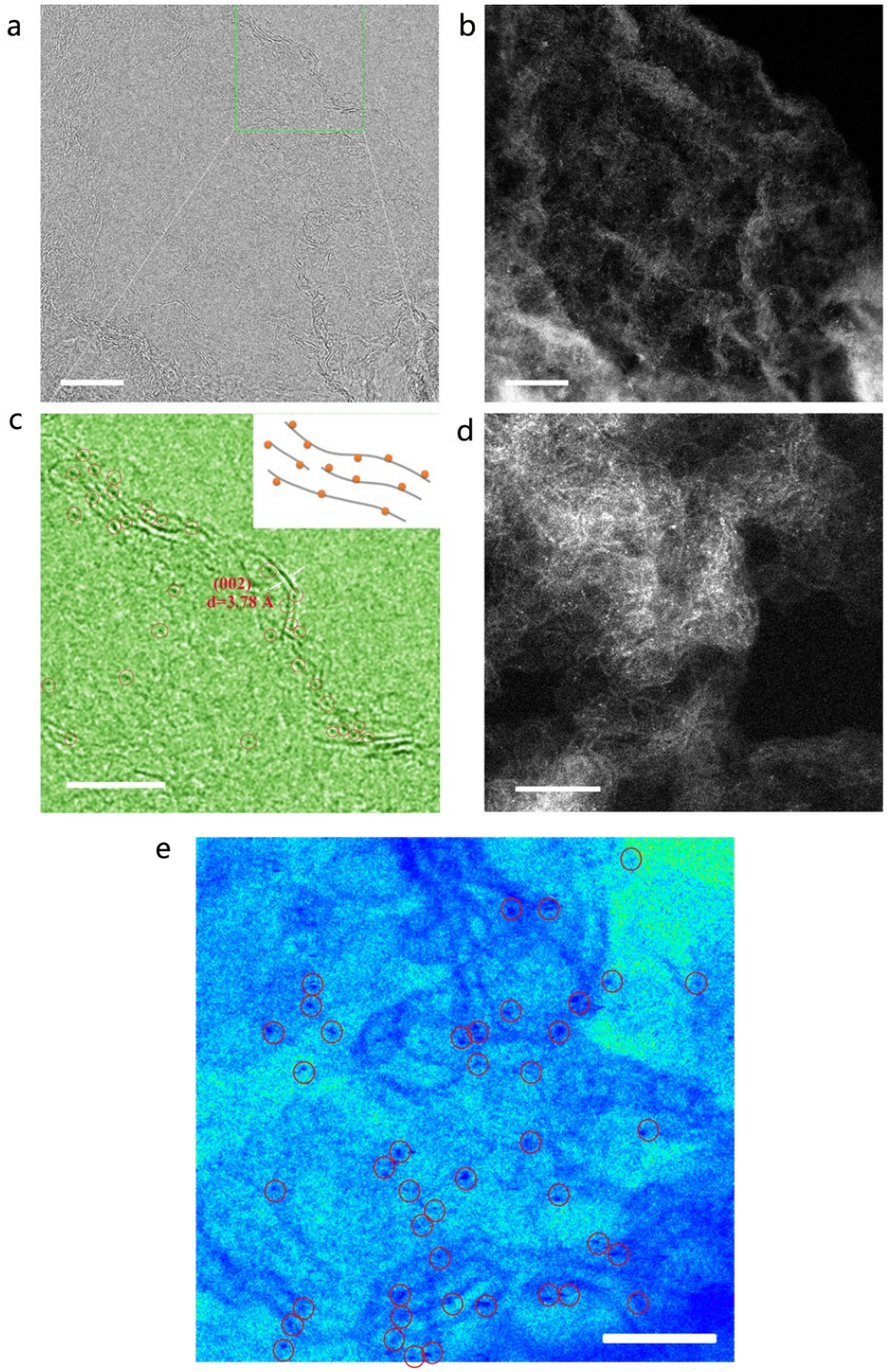

Figure S8. HR-TEM (a, c) and HAADF-STEM (b, d) images of P-SAC-NG. (e) P atoms on porous graphene sheets of Figure 2D are highlighted by circles. Scale bars are 10 nm in a & b, and 2 nm in (c), (d) & (e), respectively. Inset in (c) shows the schematic illustration of the P atoms at the edge of graphene, which expand the lattice of graphene.

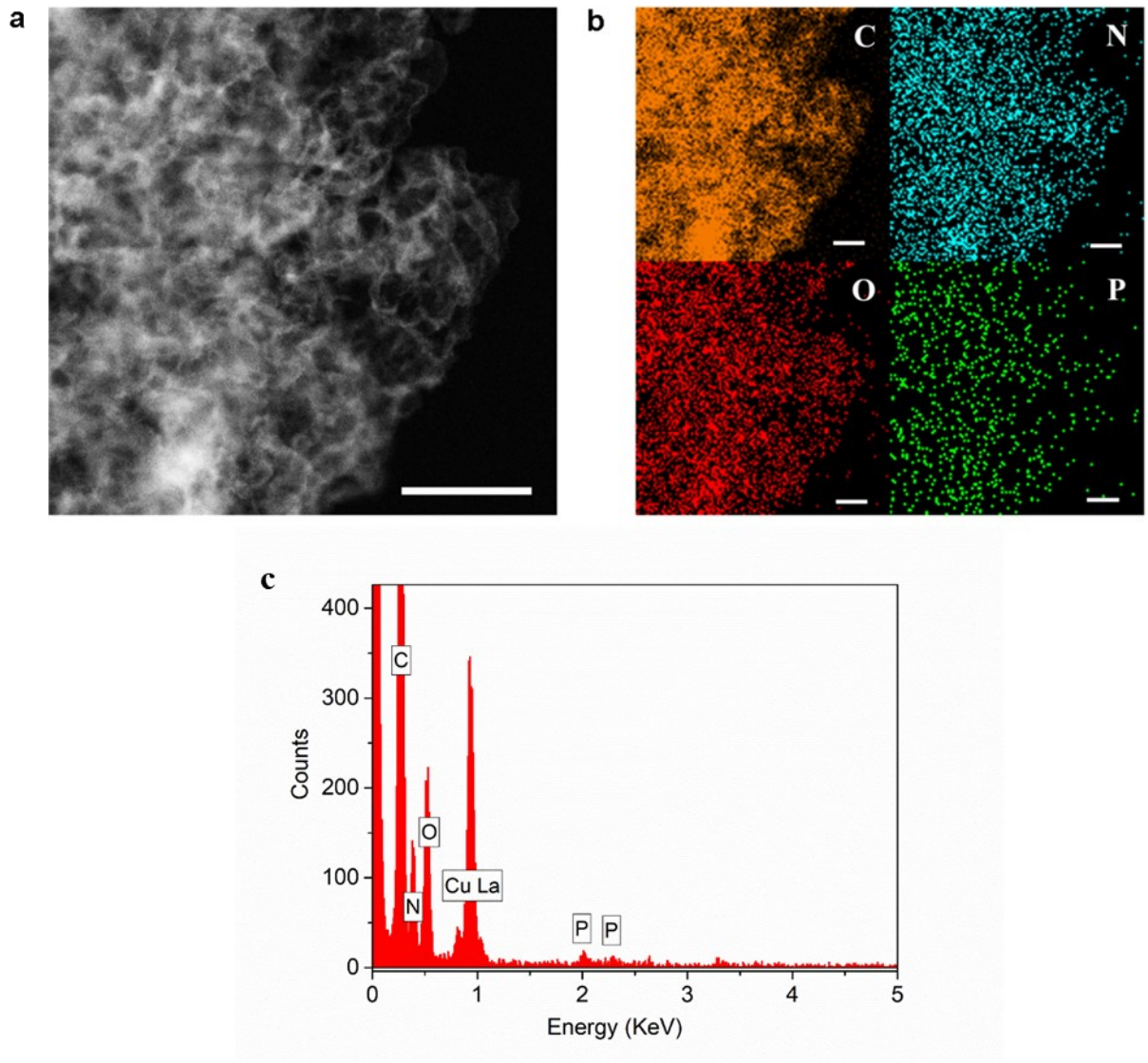

Figure S9. (a) Dark-field TEM image of P-SAC-NG and (b) the corresponding elemental mappings. Scale bars are 50 nm in (a) and (b), respectively. (c) EDX spectrum of P-SAC-NG.

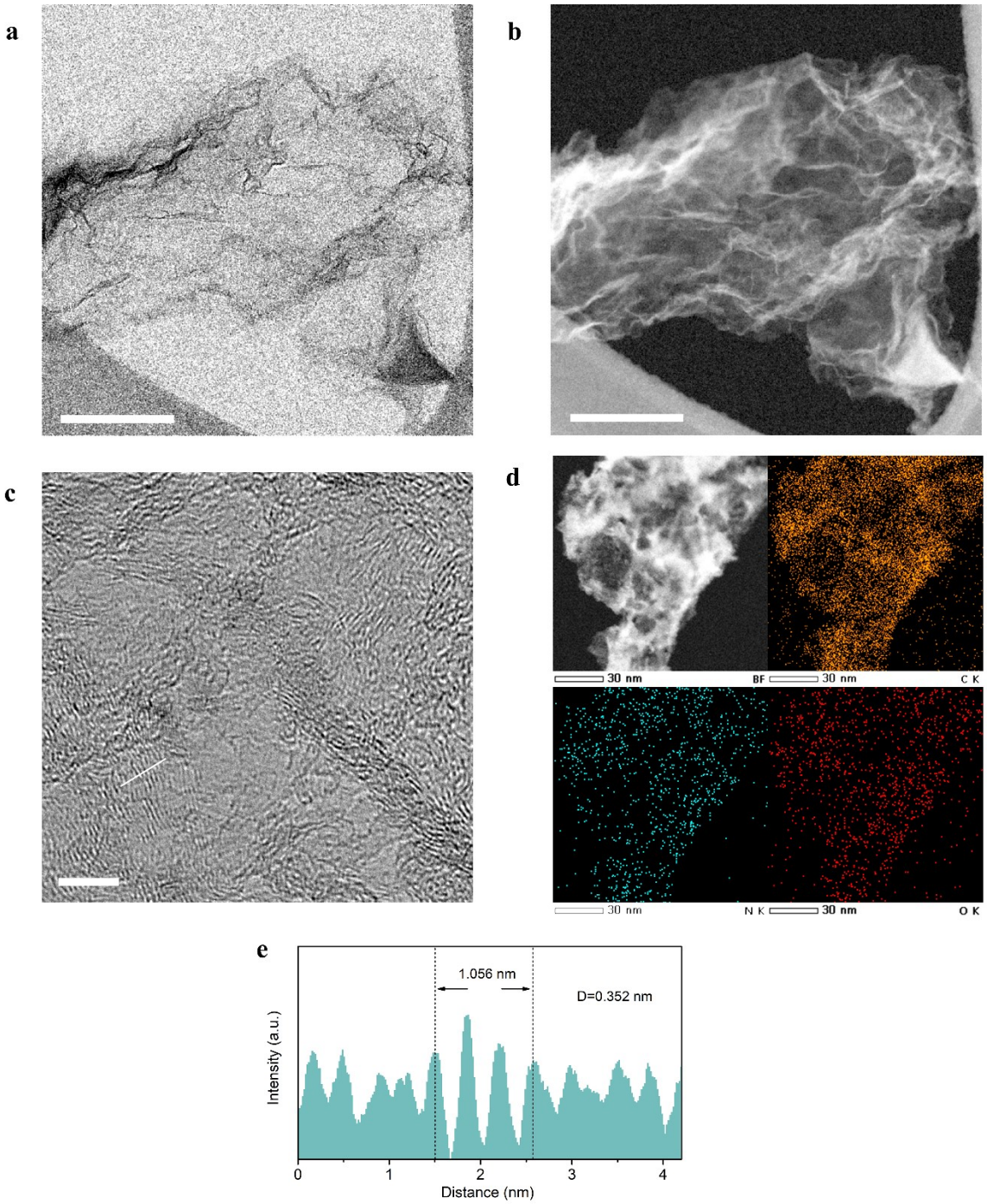

Figure S10. TEM images of NG. (a) Bright field, (b) dark field, (c) HRTEM image, (d) the corresponding elemental mappings. (e) Line (white line in c) profile showing the lattice of NG. Scale bars are 100 nm in (a), (b) and 10 nm in (c).

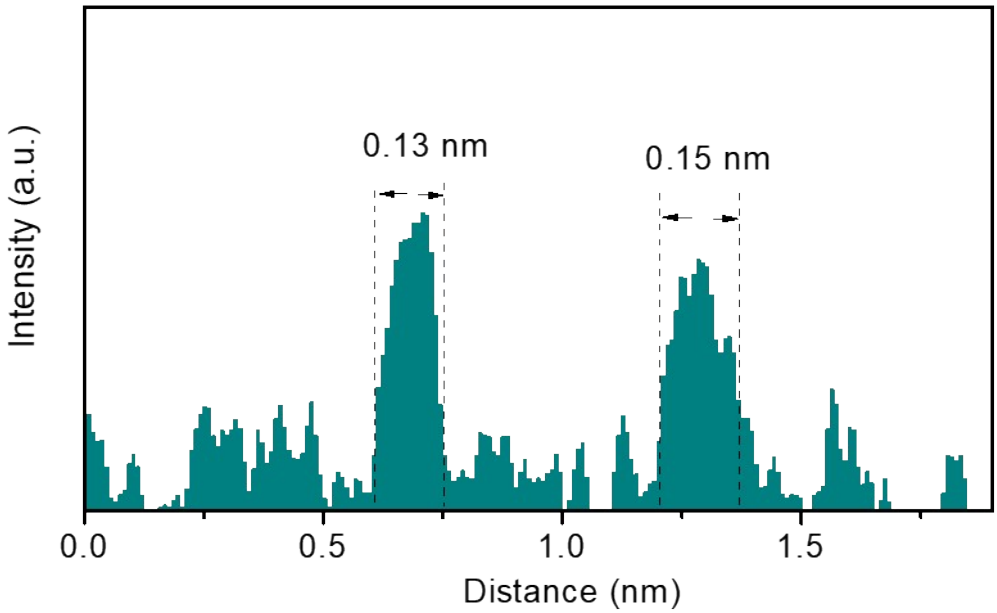

Figure S11. Line profile of single P atoms.

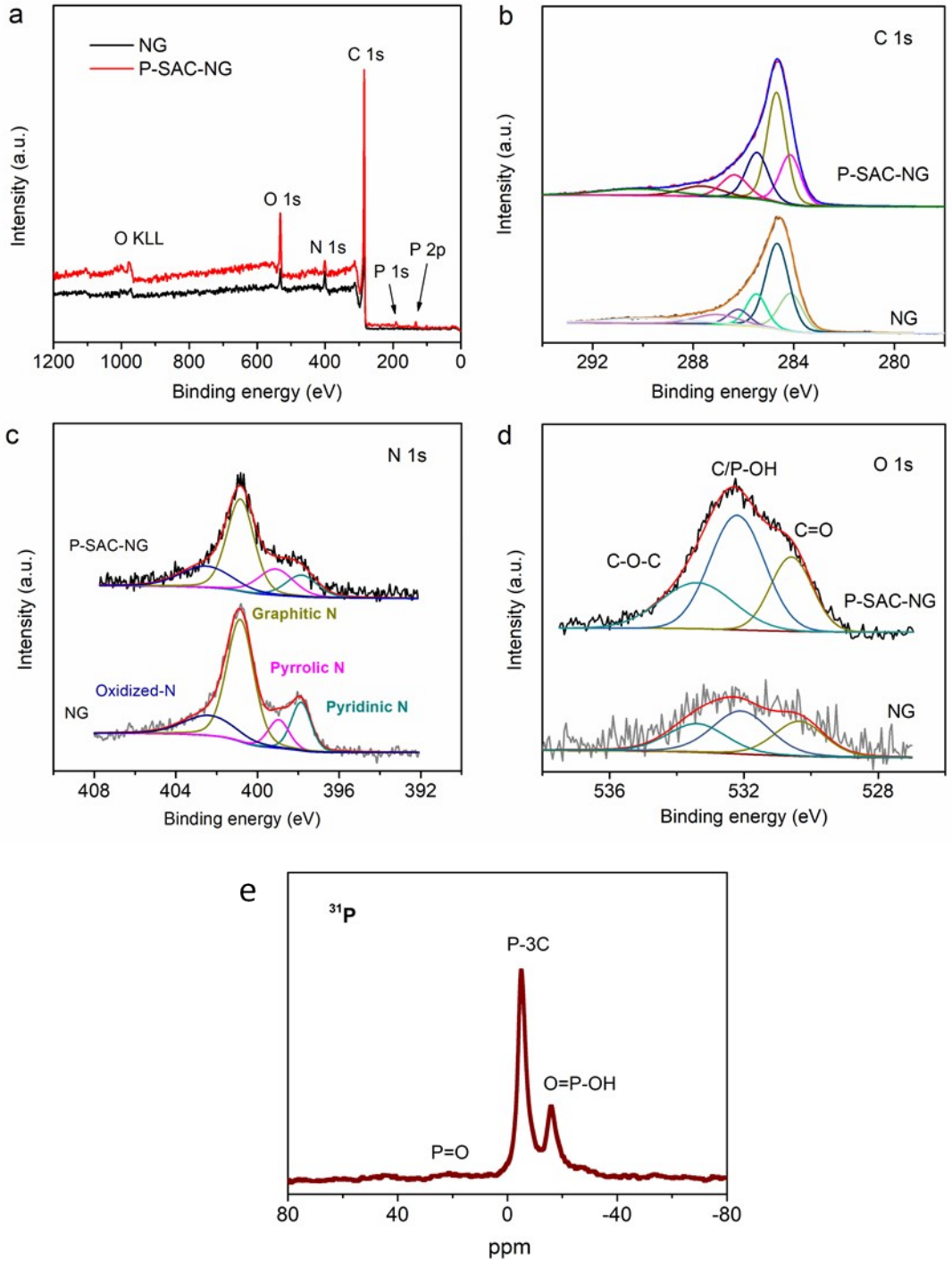

Figure S12. XPS spectra of P-SAC-NG and NG. (a) survey, (b) C 1s, (c) N 1s, and (d) O 1s. The C 1s peak can be deconvoluted into five peaks, which correspond to sp^3 carbon, sp^2 carbon, C–O, C=O (C-N, C–P) and O–C=O, respectively. (e) ^{31}P solid-state NMR of P-SAC-NG.

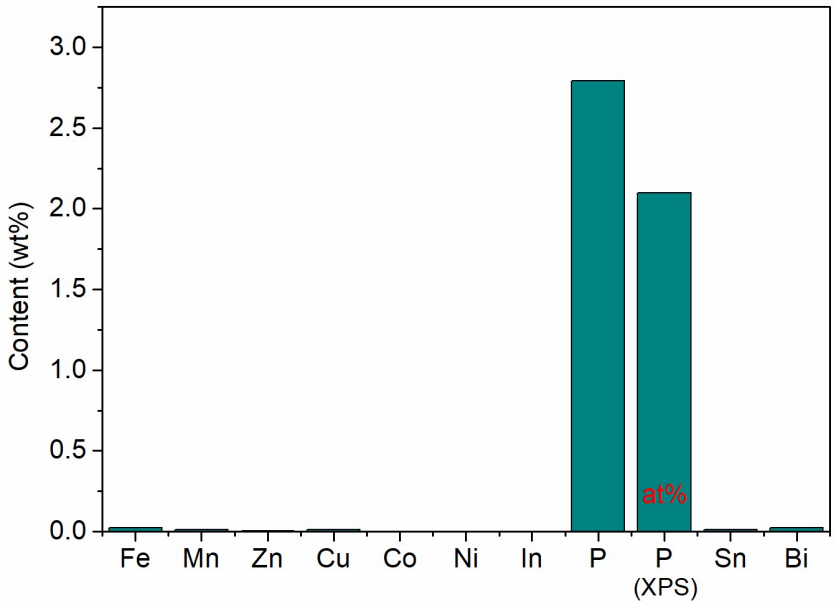

Figure S13. Content of elements in P-SAC-NG obtained from ICP-MS and XPS measurements.

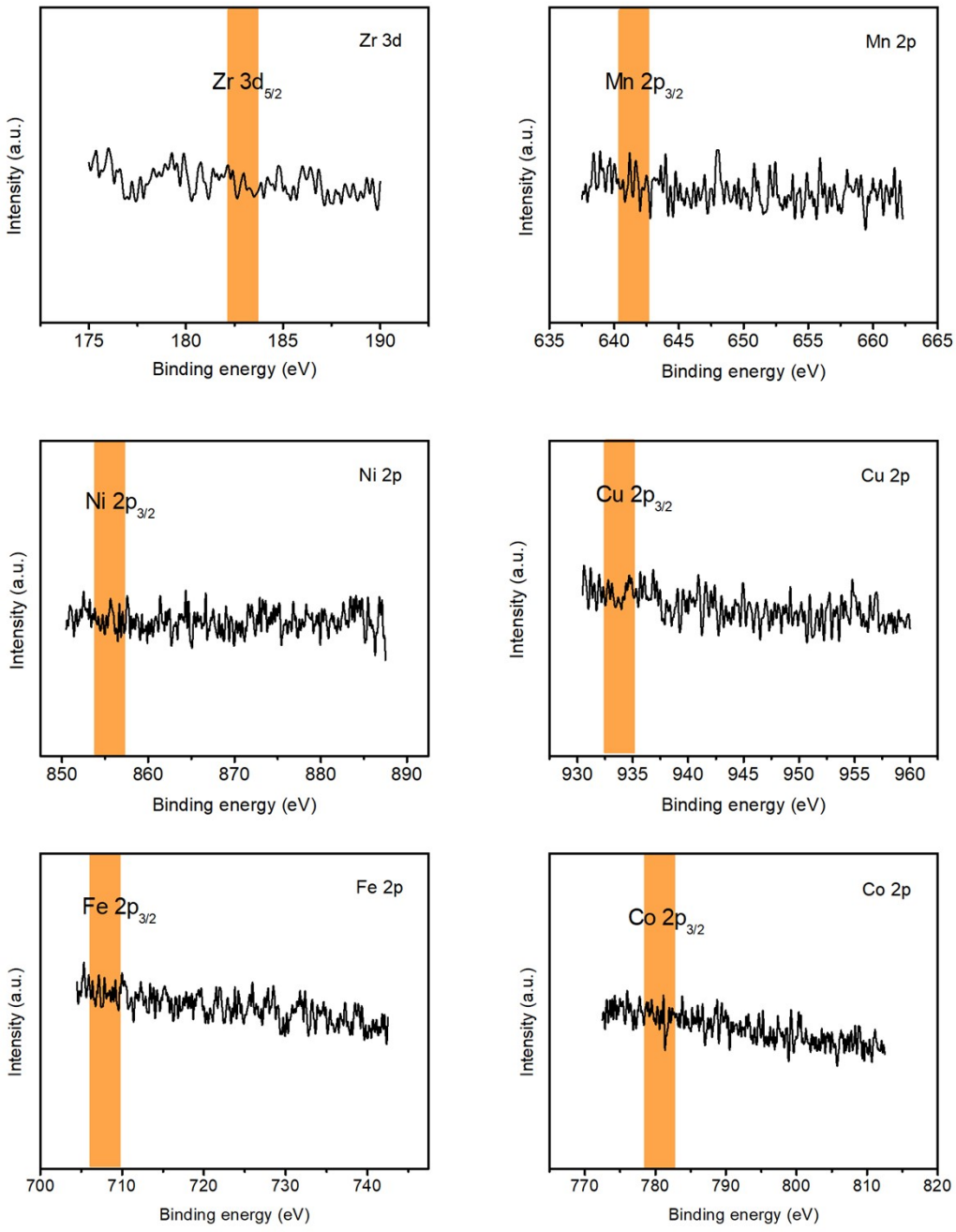

Figure S14. High resolution XPS spectra for the binding energy region of Zr 3d, Mn 2p, Ni 2p, Cu 2p, Fe 2p and Co 2p.

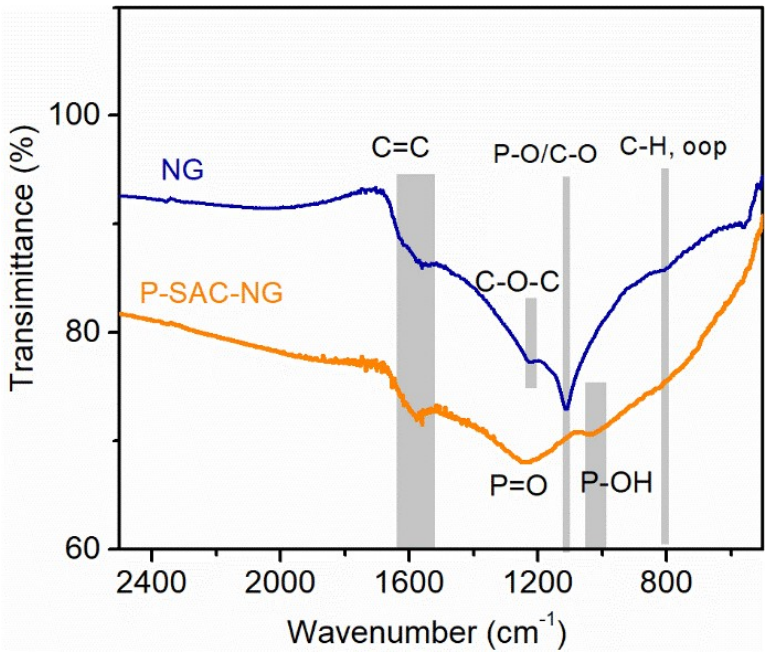

Figure S15. FTIR spectra of P-SAC-NG and NG.

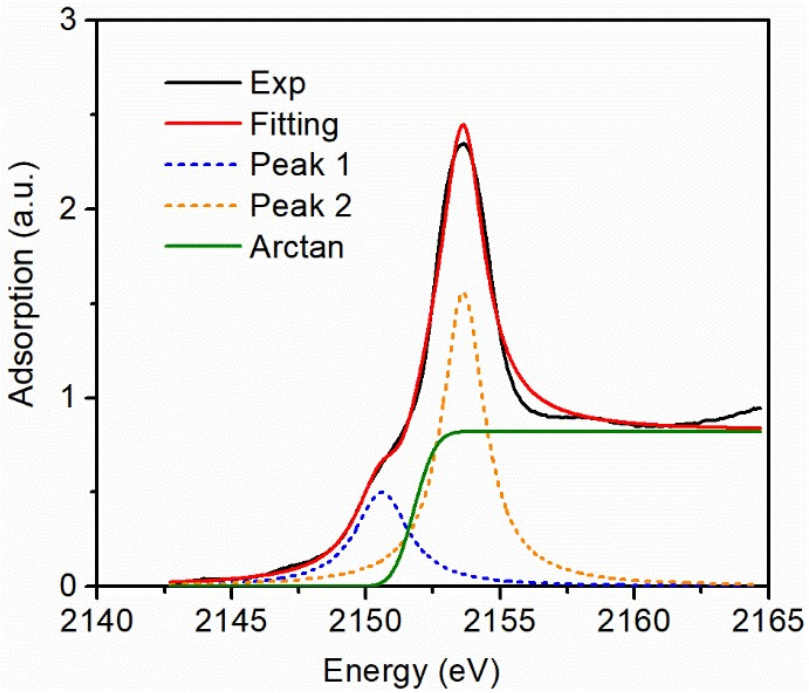

Figure S16. P K-edge XANES spectrum of P-SAC-NG, fitted by two absorption bands. Arctan is the background.

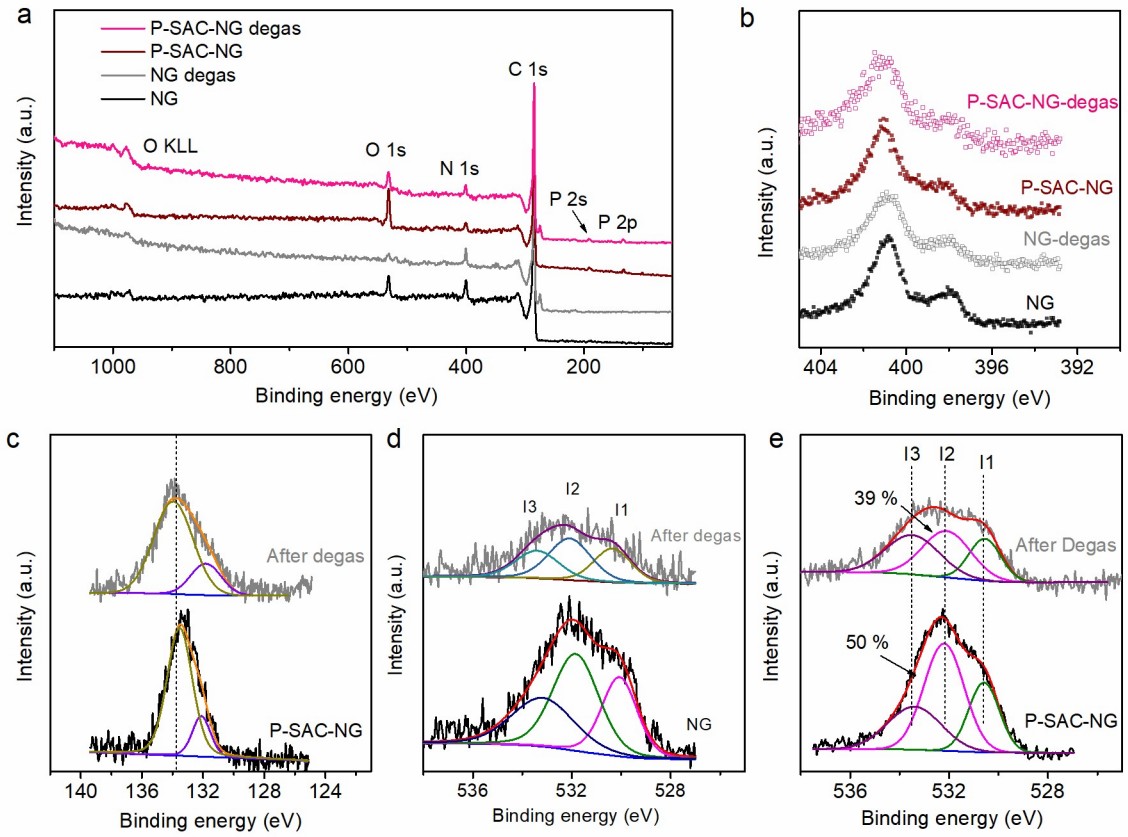

Figure S17. XPS spectra of P-SAC-NG and NG before and after treatment at 450 °C for 30 min in vacuum. (a) survey, (b) N 1s, (c) P 2p of P-SAC-NG, and O 1s of (d) NG and (e) P-SAC-NG. The I1, I2 and I3 in (d) and (e) present O double bond to aromatic C, O single bond to aliphatic C/P-OH and O single bond to aromatic C, respectively.

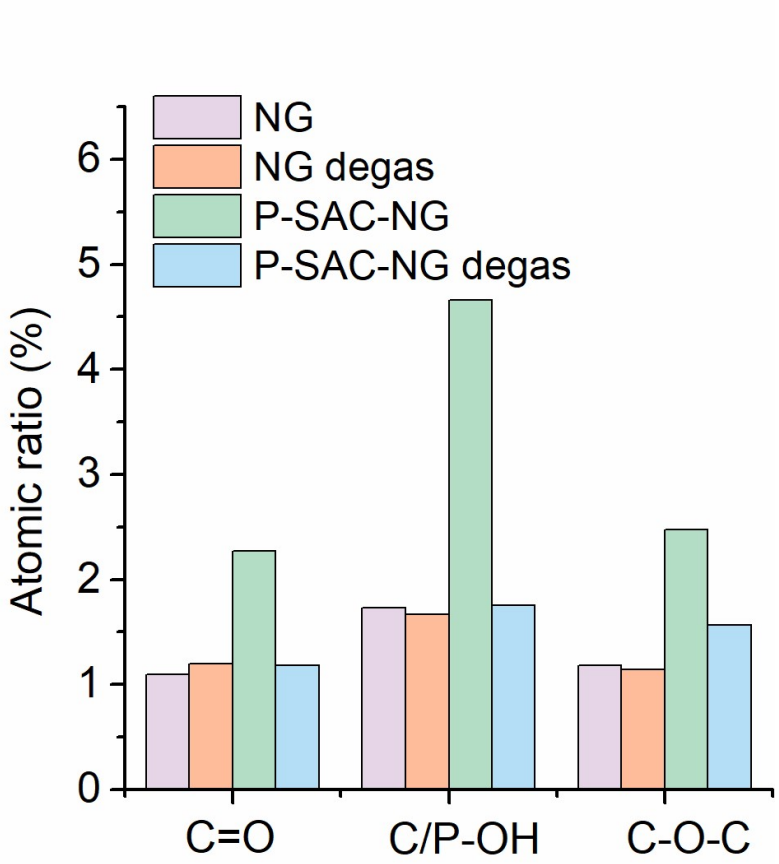

Figure S18. Comparison of O species in P-SAC-NG and NG before and after treatment at 450 °C for 30 min in vacuum.

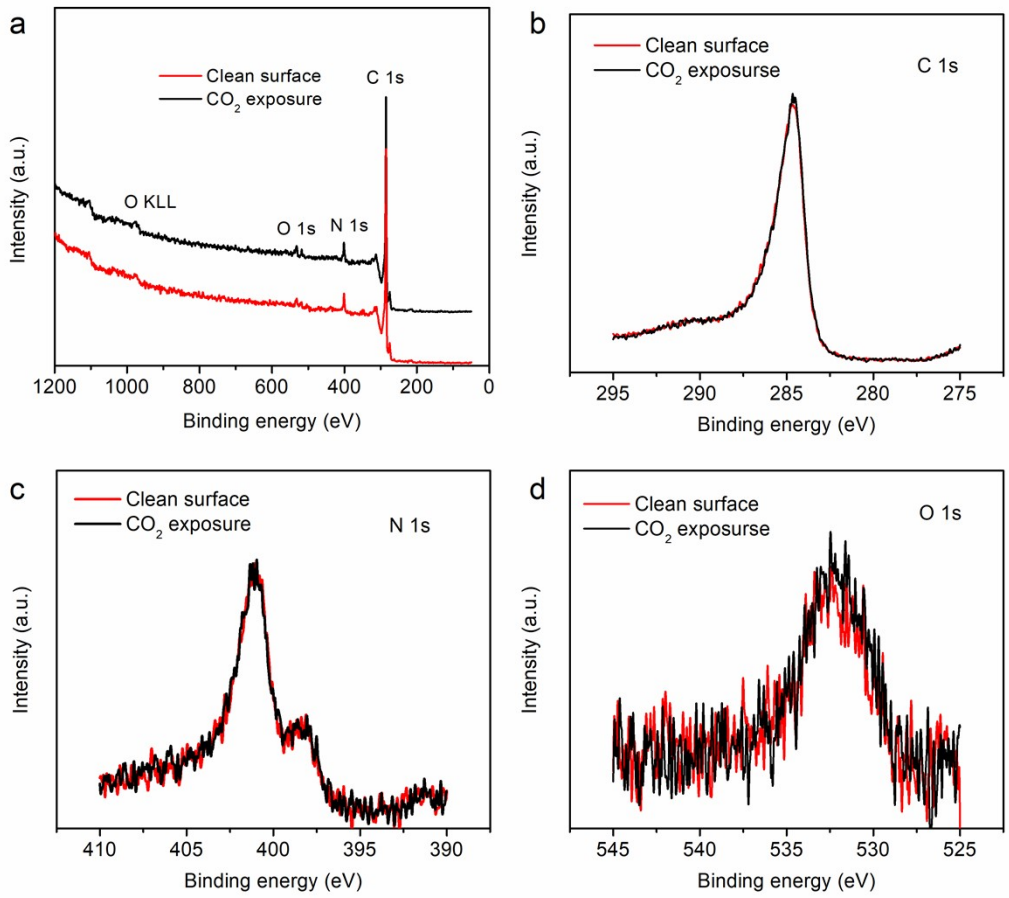

Figure S19. XPS spectra of NG before and after exposure to CO_2 gas. (a) survey, (b) C 1s, (c) N 1s and (d) O 1s.

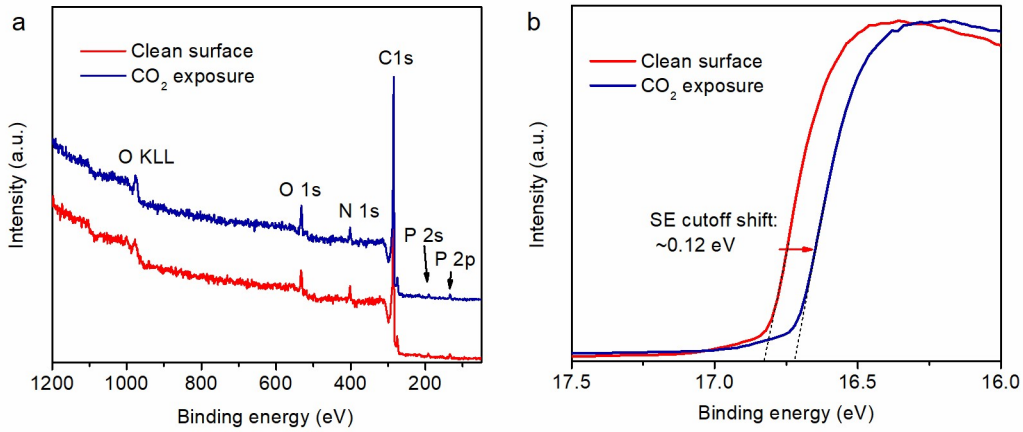

Figure S20. UPS spectra of P-SAC-NG before and after exposure to CO_2 gas. (a) survey and (b) second electron cut-off region.

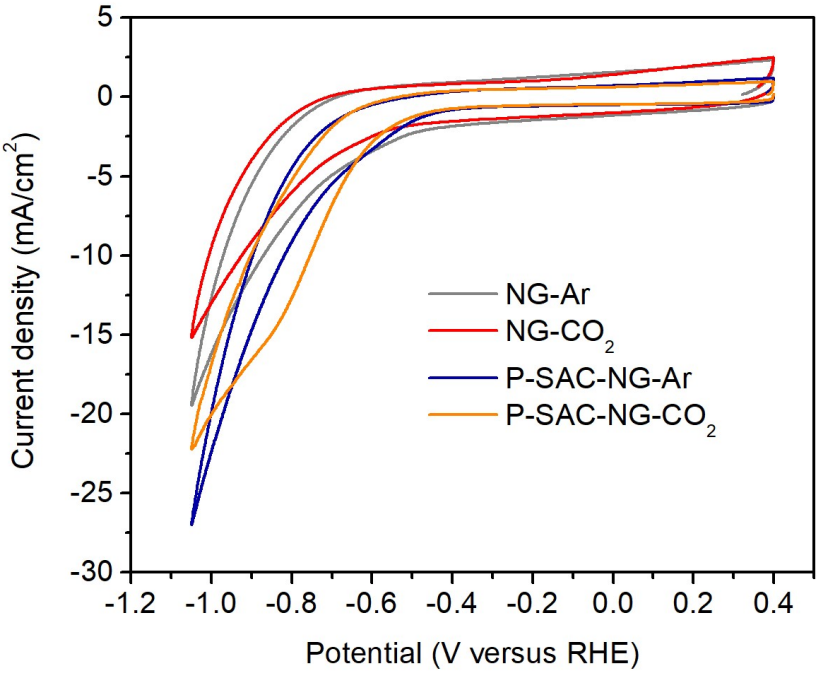

Figure S21. CV curves of P-SAC-NG and NG catalysts in Ar and CO_2 saturated 0.5 M $KHCO_3$ solution. Catalyst loading: 0.15 mg/cm^2 on glassy carbon electrode. Scan rate: 20 mV/s.

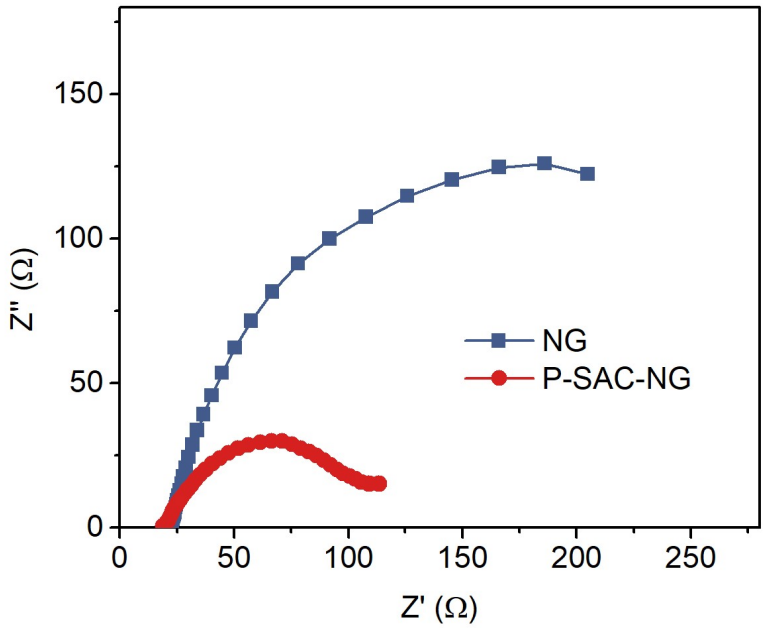

Figure S22. EIS spectra of NG and P-SAC-NG acquired in CO_2-saturated 0.5 M $KHCO_3$ solution on a rotating disc electrode at a rotation speed of 1,600 r.p.m. and a cathodic bias of -0.5 V vs. RHE.

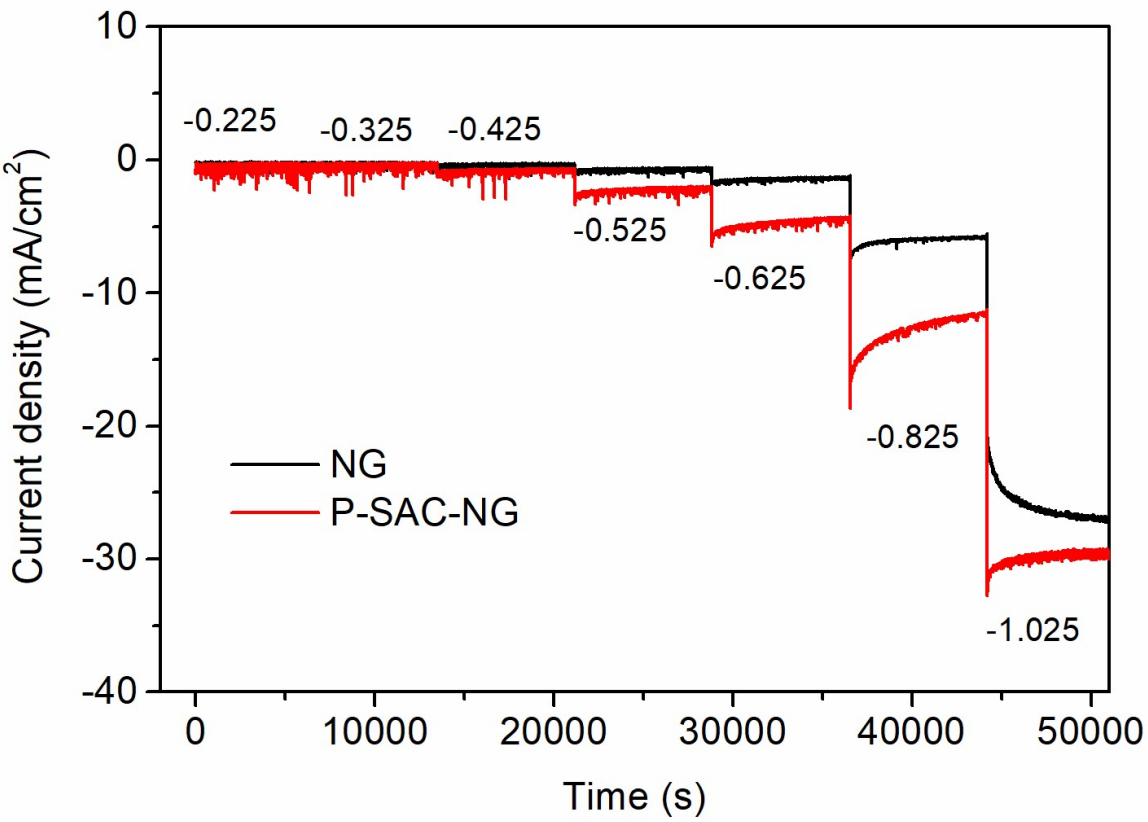

Figure S23. Current–time response of P-SAC-NG and NG catalysts on carbon fiber paper for CO_2RR product quantification at various bias potentials. The number labelled in the figure shows the applied potential on the electrode in the unit of V versus RHE.

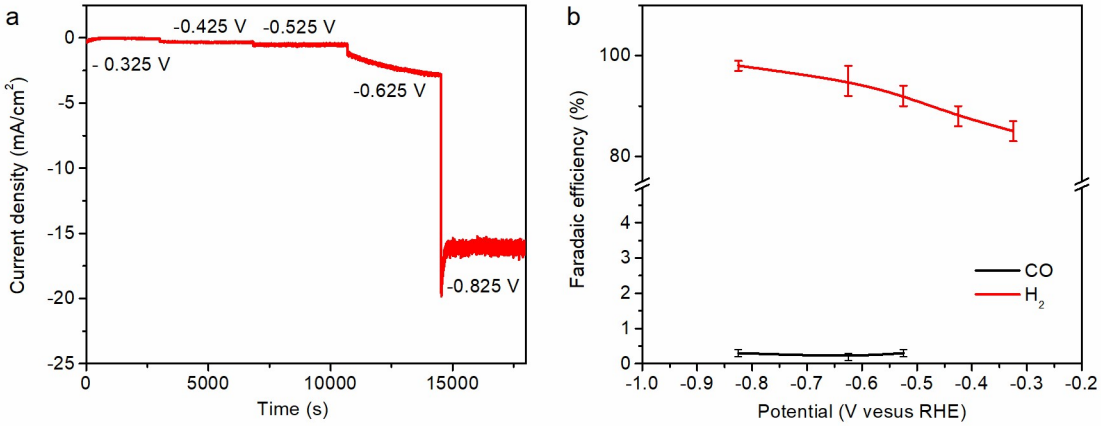

Figure S24. (a) Current–time response and (b) Faradaic efficiency of carbon fiber paper for CO_2RR. The number labelled in the figure shows the applied potential on the electrode in the unit of V versus RHE.

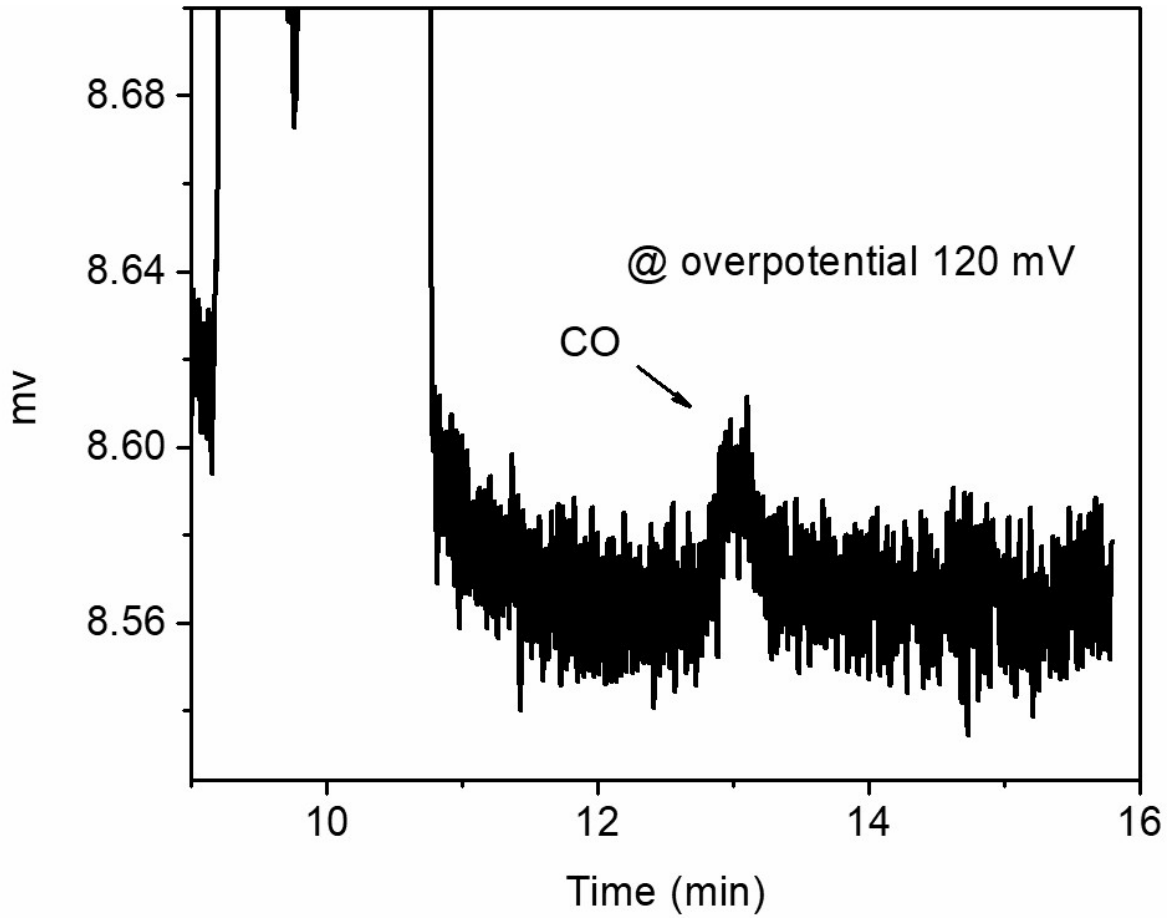

Figure S25. FID signal recorded for the P-SAC-NG electrode at an overpotential of 120 mV in 0.5 M CO_2 saturated $KHCO_3$ aqueous solution with an electrode area of 2 cm^2.

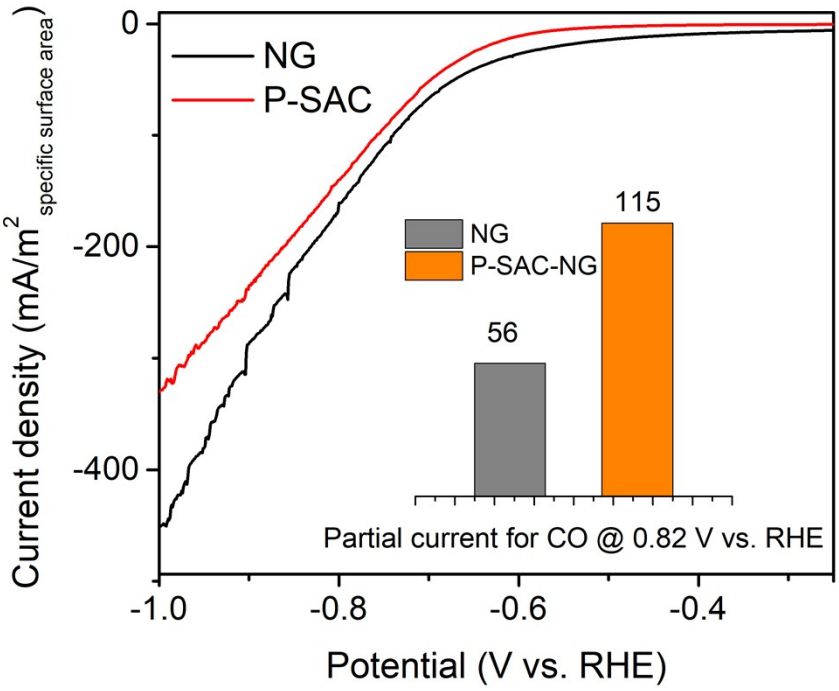

Figure S26. (a) Normalized LSV curves for the catalysts acquired in CO_2-saturated 0.5 M $KHCO_3$ solution on a rotating disc electrode at a rotation speed of 1,600 r.p.m. and a scan rate of 5 mV s-1. Inset shows the partial current density of CO_2RR to CO at -0.82 V vs. RHE.

Note: As shown in Figure S26, after specific surface area normalization, the total CO_2RR current density for P-SAC-NG is slightly smaller than that for NG. However, after considering the selectivity of CO_2RR, the partial current density of CO_2RR to CO over P-SAC-NG is still much higher as compared to that over NG at the same applied potential (inset in Figure 26).

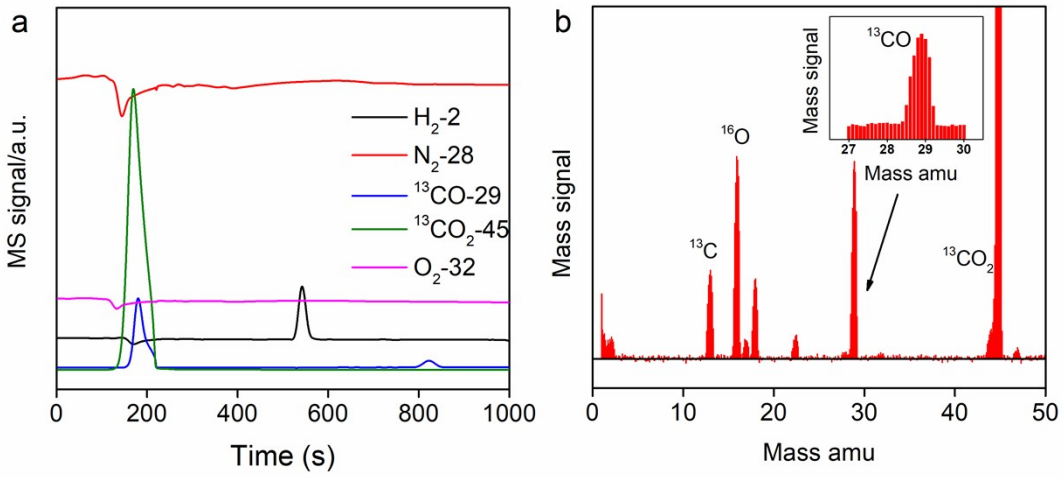

Figure S27. Gas chromatography mass spectra recorded with $^{13}CO_2$ as the feed reactant for CO_2RR.

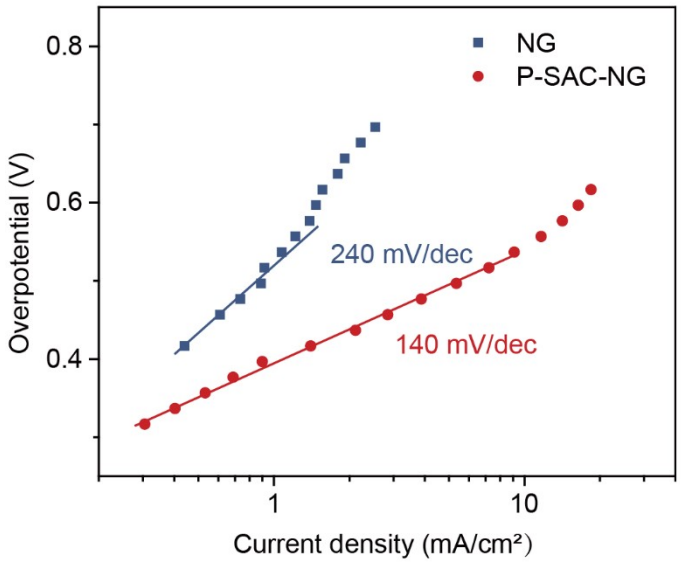

Figure S28. Tafel plots of CO_2RR for NG and P-SAC-NG.

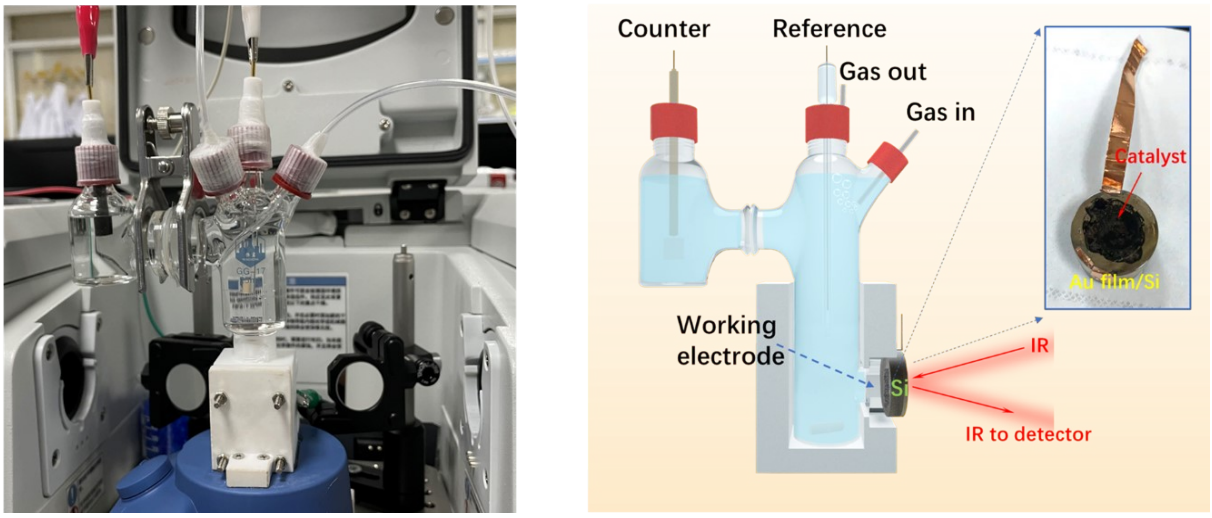

Figure S29. Digital photograph and schematics showing the ATR-SEIRAS set-up.

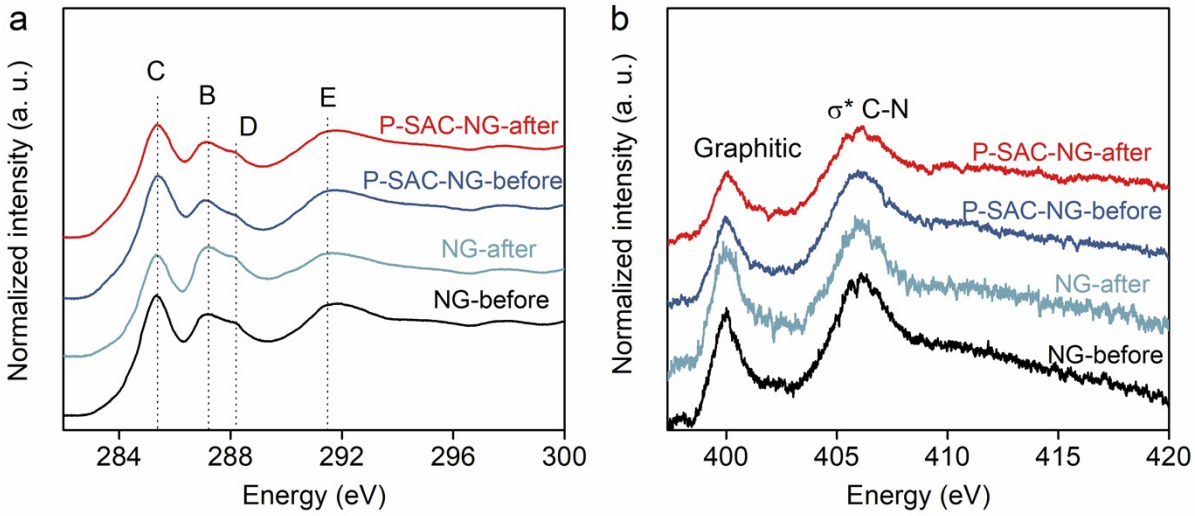

Figure S30. (a) C and (b) N K-edge XANES spectra before and after CO_2RR for P-SAC-NG and NG catalysts. In the carbon K-edge XANES spectra, A: defects, B: π* C=C, C: π* C–OH, D: π* C–O–C, C–N, and E: σ* C–C.

Note: The variation of the carbon K-edge XANES of NG is larger than that of P-SAC-NG before and after CO_2RR, suggesting more carbon atoms in NG participated in the CO_2RR, in line with the previous understanding that the carbon atoms adjacent to the doped nitrogen species are the active sites in electrochemical CO_2RR.

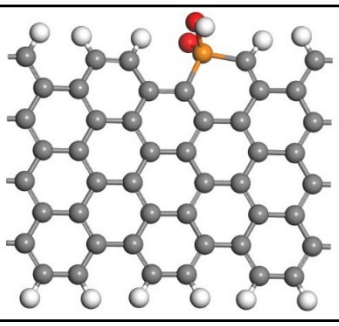	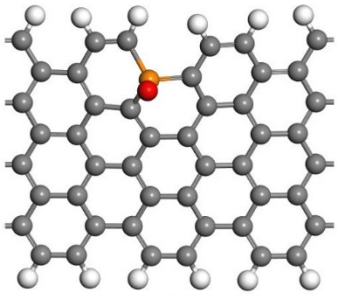	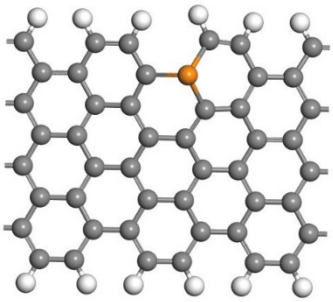
A: 2C-P=O(OH)	B: 3C-P=O	C: 3C-P
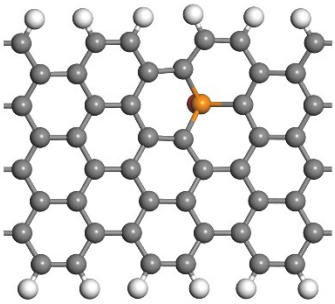	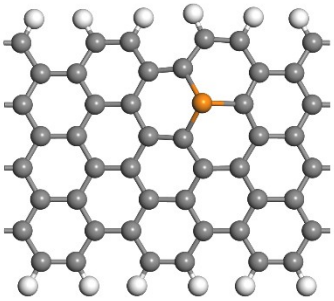	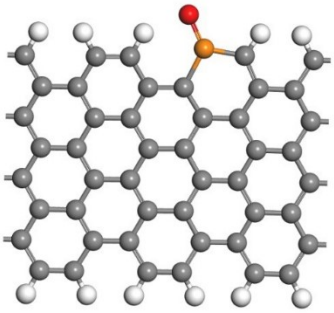
D: 3C-P=O	E: 3C-P	A1: 2C-P=O
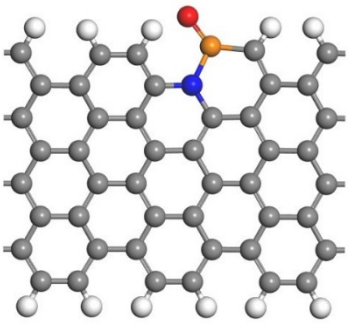	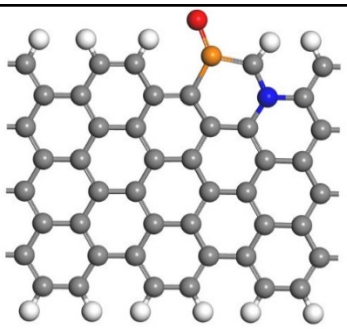	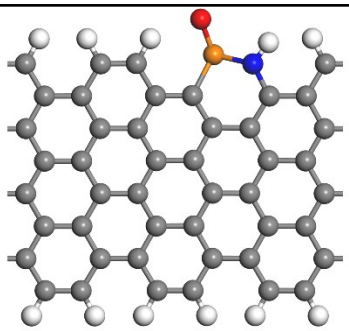
A2: CN-P=O	A3: (N)2C-P=O	A4: CN-P=O
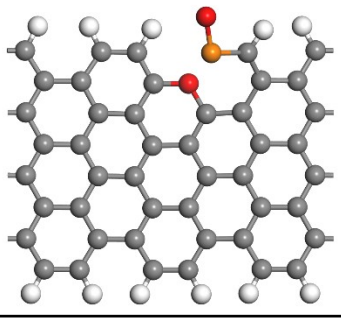	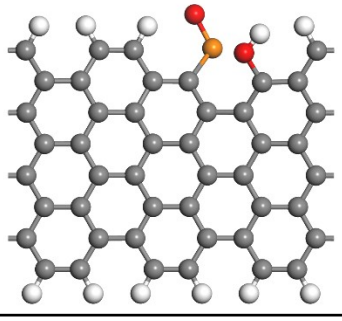	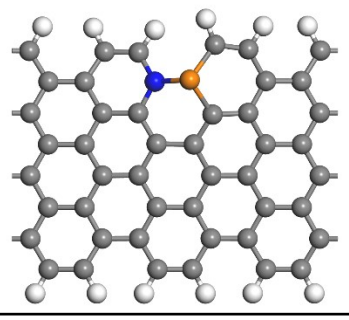
A5: CO-P=O	A6: CO-P=O	C1: 2CN-P

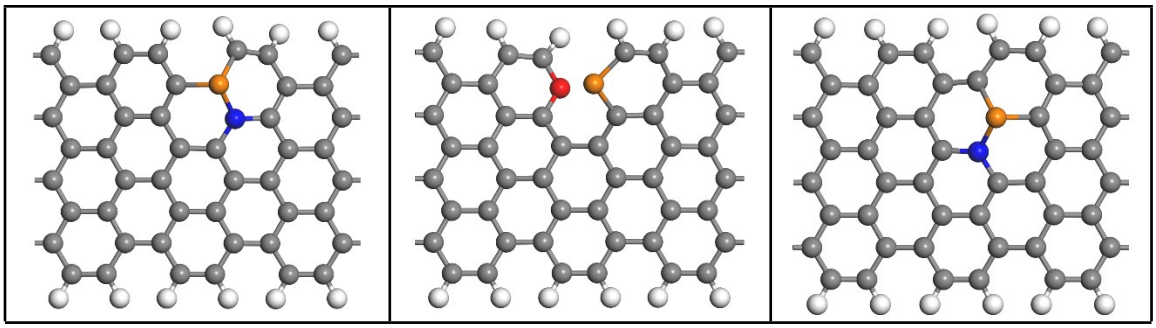

Figure S31. Various possible configurations of P atom on graphene (at the armchair or basal plane). The influence of N incorporation and the coordination interactions of P atom were examined. Gray, white, red, yellow and blue spheres represent C, H, O, P and N, respectively.

	*COOH	*CO
A (*P)	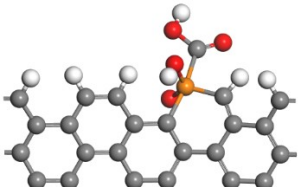 ΔG = 3.14 eV	
A (*C)	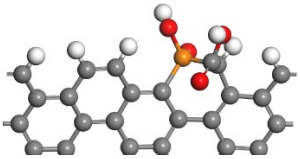 ΔG = 0.35 eV	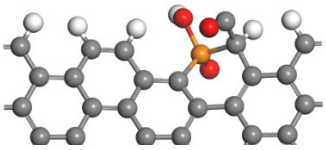 ΔG = 1.72 eV
A (*C′)	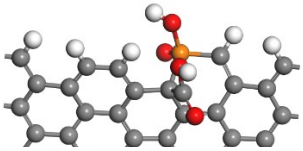 ΔG = 1.09 eV	
B (*P)	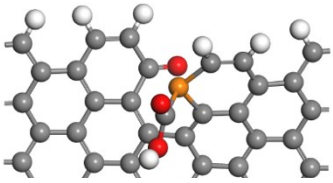 ΔG = 2.45 eV	
C (*P)	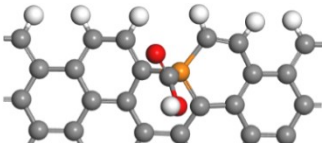 ΔG = 1.05 eV	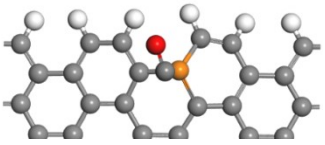 ΔG = 1.14 eV
D (*P)	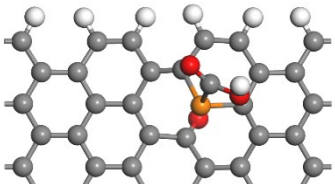 ΔG = 3.02 eV	
E (*P)	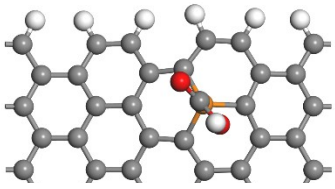 ΔG = 0.74 eV	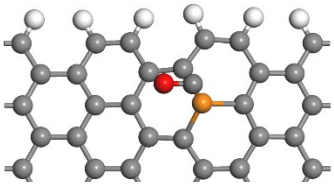 ΔG = 1.12 eV
C1 (*P)	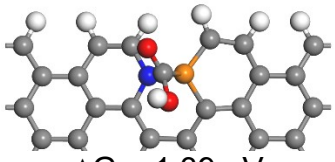 ΔG = 1.39 eV	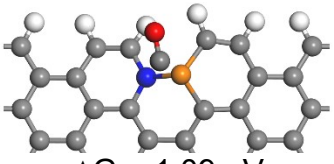 ΔG = 1.09 eV

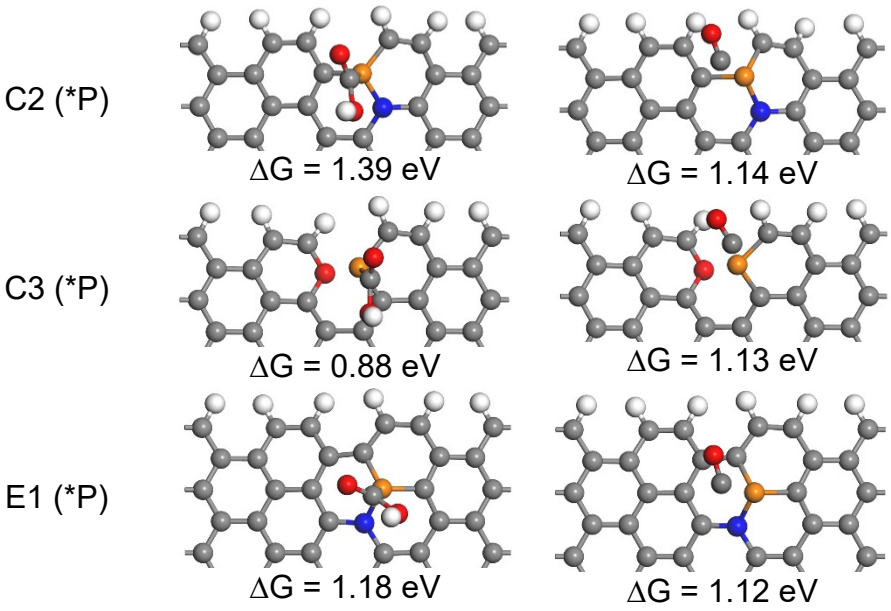

Figure S32. Optimized configurations and binding energies of *COOH and *CO adsorbed on the single atomic P site and C site for different models (A: 2C-P=O(OH), B: 3C-P=O, C: 3C-P). Gray, white, red, yellow and blue spheres represent C, H, O and P, respectively.

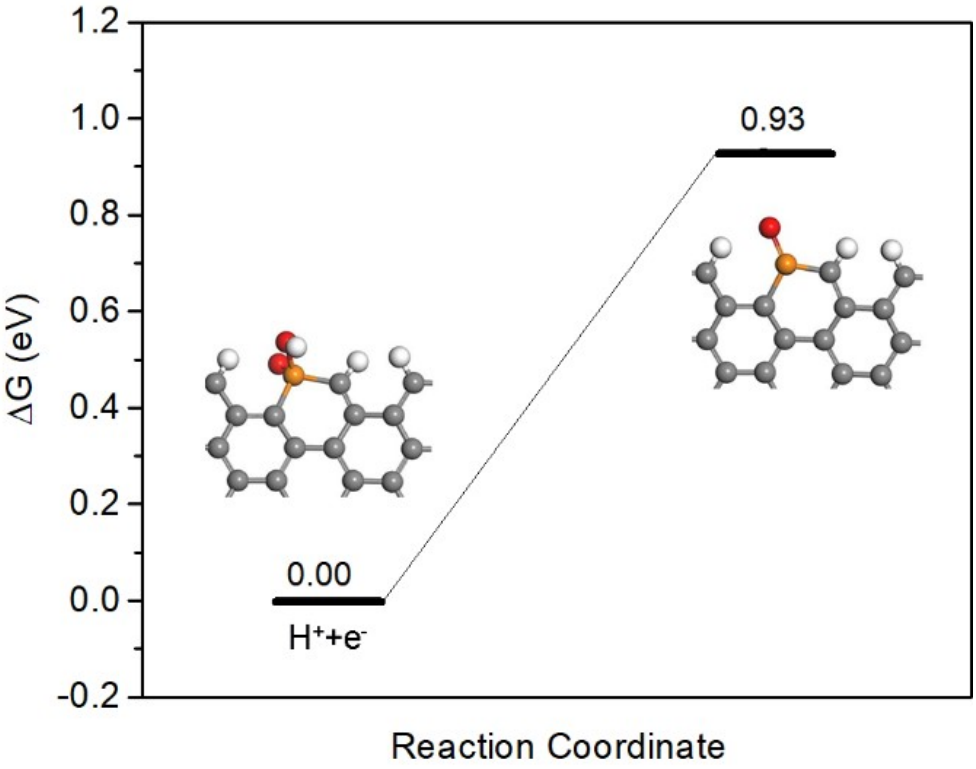

Figure S33. Gibbs free energy diagram of the PCET step showing 2C-P=O(OH) transfer to 2C-P=O configuration. Gray, white, red, yellow and blue spheres represent C, H, O and P, respectively. Note: this PCET step ($-OH+H^{+}+e^{-}\rightarrow H_2O$) is consistent with that of observation in the O K-edge XANES differential spectra of Fig. 5b.

	*COOH	*CO
A1 (*P)	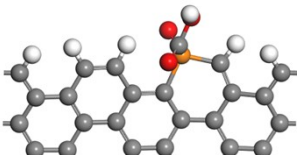 ΔG = 0.64 eV	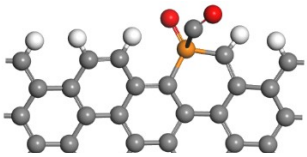 ΔG = 0.93 eV
A1 (*C)	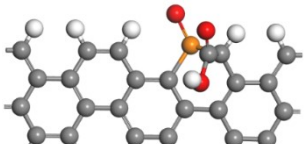 ΔG = 0.93 eV	
A1 (*C′)	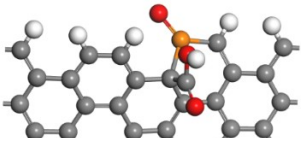 ΔG = 1.54 eV	
A2 (*P)	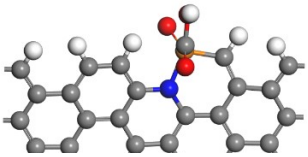 ΔG = 0.26 eV	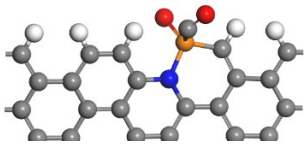 ΔG = 1.19 eV
A2 (*N)	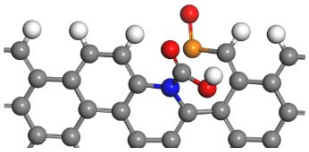 ΔG = 1.60 eV	
A2 (*C)	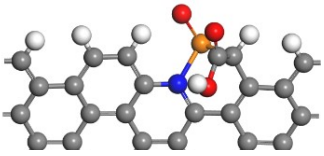 ΔG = 0.11 eV	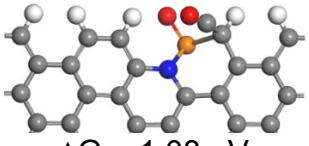 ΔG = 1.08 eV
A3 (*P)	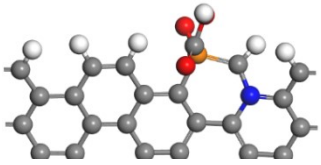 ΔG = 0.47 eV	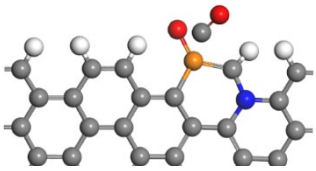 ΔG = 0.81 eV
A3 (*C)	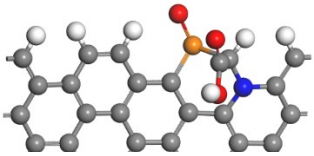 ΔG = 0.47 eV	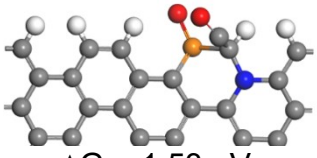 ΔG = 1.53 eV
A3 (*C′)	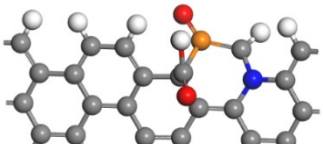	

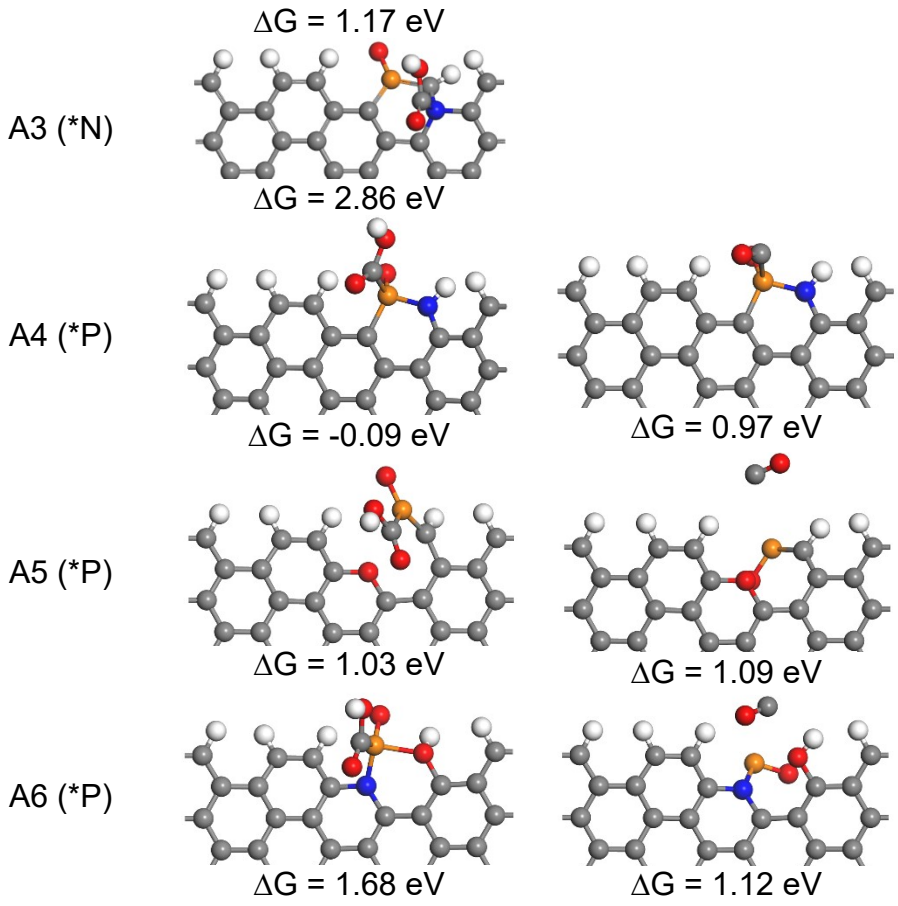

Figure S34. Gibbs free energy of CO_2RR at the P, C and N sites for A1-A6. Gray, white, red, yellow and blue spheres represent C, H, O, P and N, respectively.

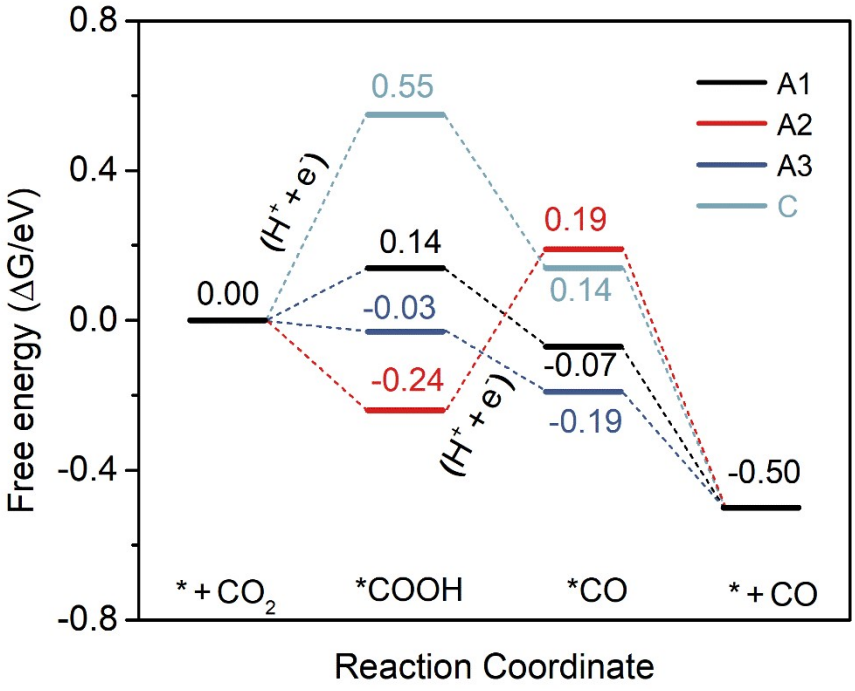

Figure S35. The energy barrier of CO_2RR for A1-A3 and C configurations at the applied potential of U = -0.5 V.

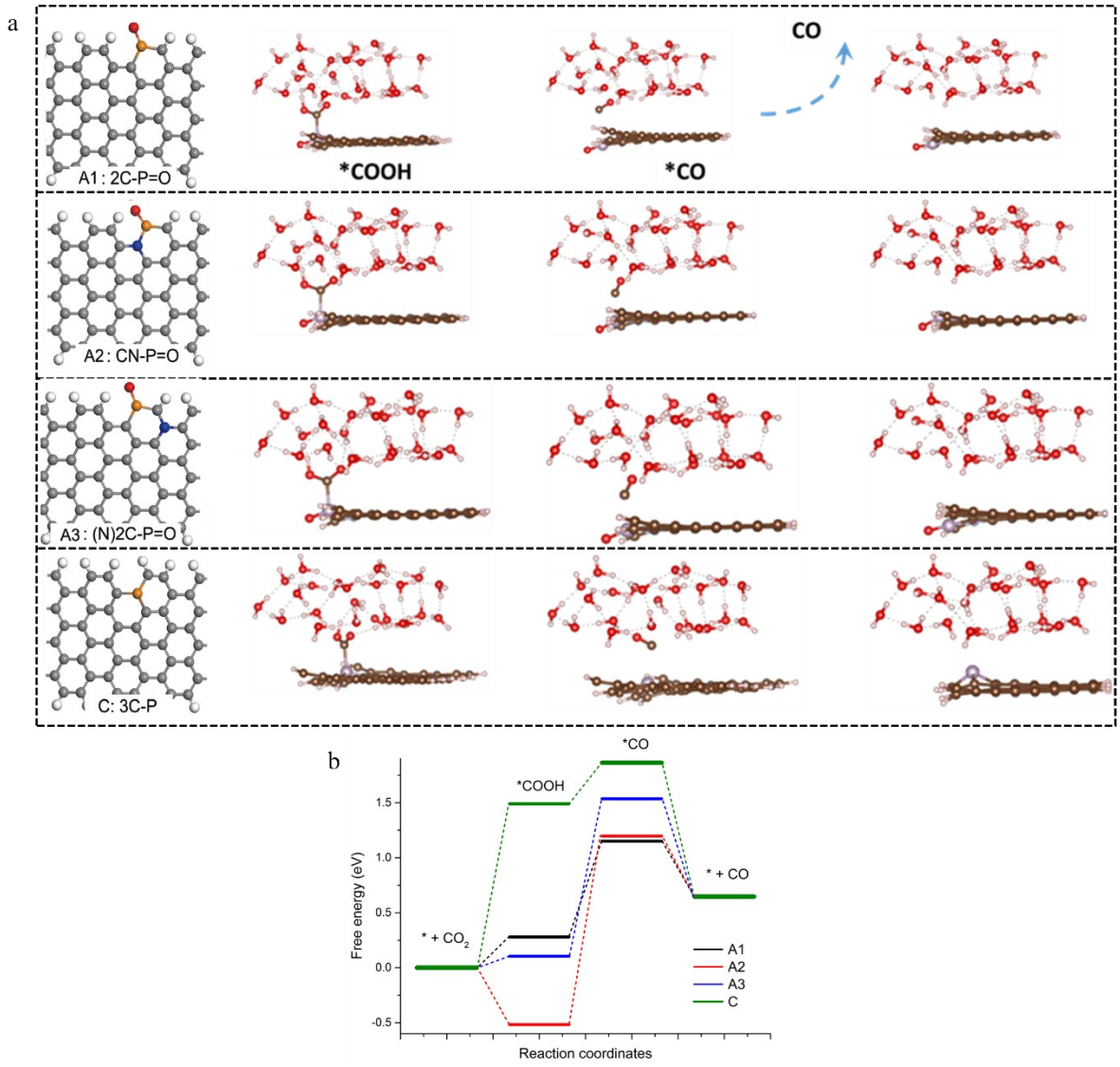

Figure S36. (a) Different configurations of P atom optimized by DFT calculation. A1: 2C-P=O, A2: CN-P=O, A3: (N)2C-P=O, and C: 3C-P. Gray, white, red, yellow and blue spheres represent C, H, O, P and N, respectively. A layer of water was added over catalyst's surface to investigate the solvent effects. (b) Gibbs free energy profile for the CO_2RR on A1, A2, A3, and C, with considering solvent effects.

Note：the effects of water molecule on CO_2RR for different configurations of P atom (A1, A2, A3 and C) were investigated. The optimized structures of $*CO_2$, *COOH and *CO over A1, A2, A3 and C configurations are shown in Figure S36. Gibbs free energy profiles for the CO_2RR on A1, A2, A3, and C with consideration of a water layer are shown in S36. After considering the effects of solvent, the free energy of intermediates for CO_2RR over A1, A2, A3 and C exhibit a

dramatic change as shown in S36, but the conclusion on the catalytic trend for different P configurations is similar to the case without considering solvent effects. Without considering solvent effects, the catalytic trend for CO_2RR to CO over A1, A2, A3, and C is A3 (0.47 eV), A1 (0.64 eV) >A2 (0.93 eV), C (1.05 eV); after including solvent effects, the catalytic trend for CO_2RR to CO over A1, A2, A3, and C is A1 (0.87 eV) >A3 (1.4 eV) > C (1.49 eV), A2 (1.71 eV). In both conditions (with and without considering solvent effects), the P sites with C2-P(O) feature are identified as the catalytic site for CO_2RR to CO.

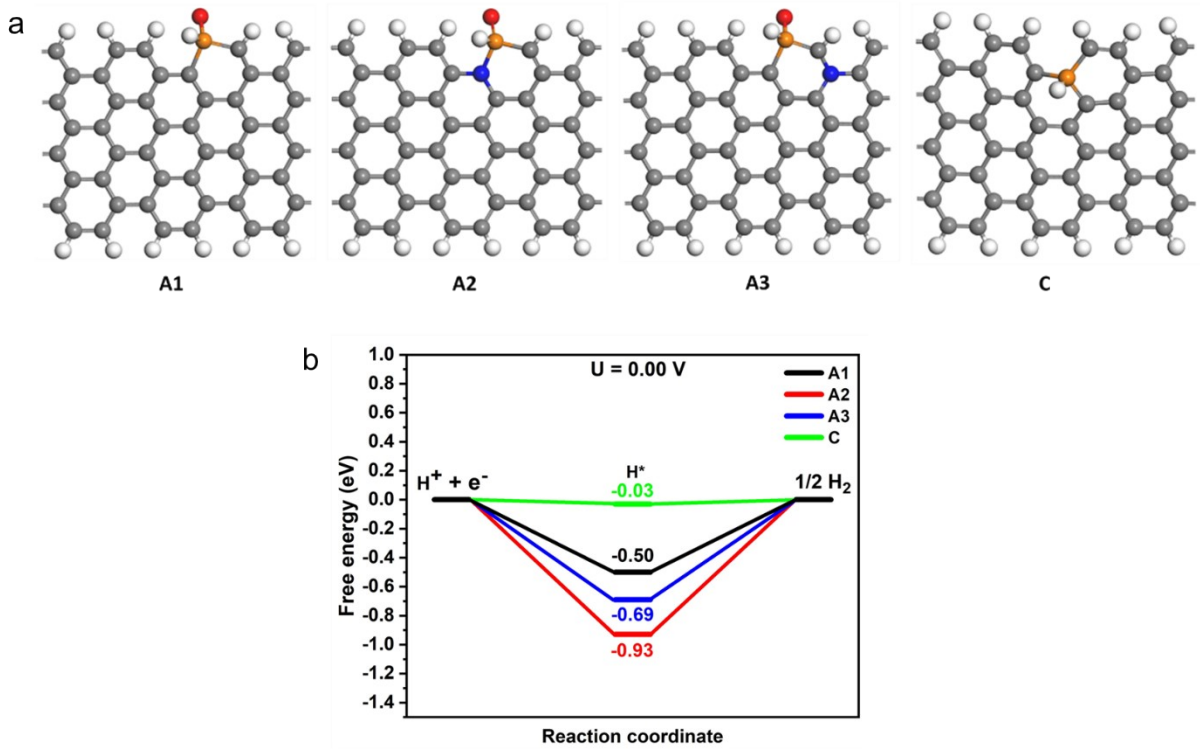

Figure S37. (a) Hydrogen adsorption sites and configurations on A1, A2, A3 and C sites, and (b) the calculated free energy (ΔG_{H^*}) diagram for HER at U = 0 V. Gray, white, red, yellow and blue spheres represent C, H, O, P and N, respectively.

Note: the CO_2RR and HER on P sites of different configurations (A1-A3 and C) were analyzed by comparing the free energy of *COOH and H* adsorption. As shown in Figures 5E and S33, the free energy of the first electron reduction of CO_2 to *COOH on P atomic site of A3 configuration is 0.47 eV, which is lower than that for H* adsorption (0.69 eV, same as the desorption energy of H_2) on P site of A3 configuration, indicating favorable CO_2 reduction reaction on P site of A3 configuration. While for other P sites, the H* adsorption energies on P sites of A1, A2 and C configurations are 0.5, 0.93 and 0.03 eV, which are lower than those of the energy barriers of the potential limited step for CO_2RR (A1: 0.64 eV for *COOH formation, A2: 0.93 eV for *CO formation and A3: 1.05 eV for *COOH formation), indicating favorable HER on P sites of A1, A2 and C configurations. Combining the structure characterizations, electrochemical performance evaluations and DFT calculations, the P site of A3 configuration is most likely the catalytic site for highly selective CO_2RR to CO.

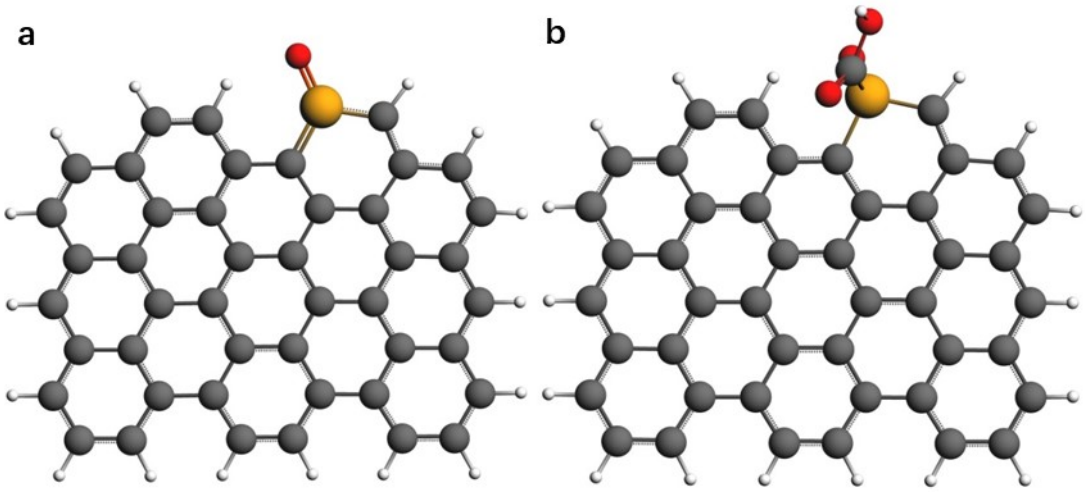

Figure S38. Optimized structures of (a) P-SAC-NG and (b) *COOH intermediate on P-SAC-NG using the cluster model. Black, gray, red and yellow spheres represent C, H, O, and P, respectively.

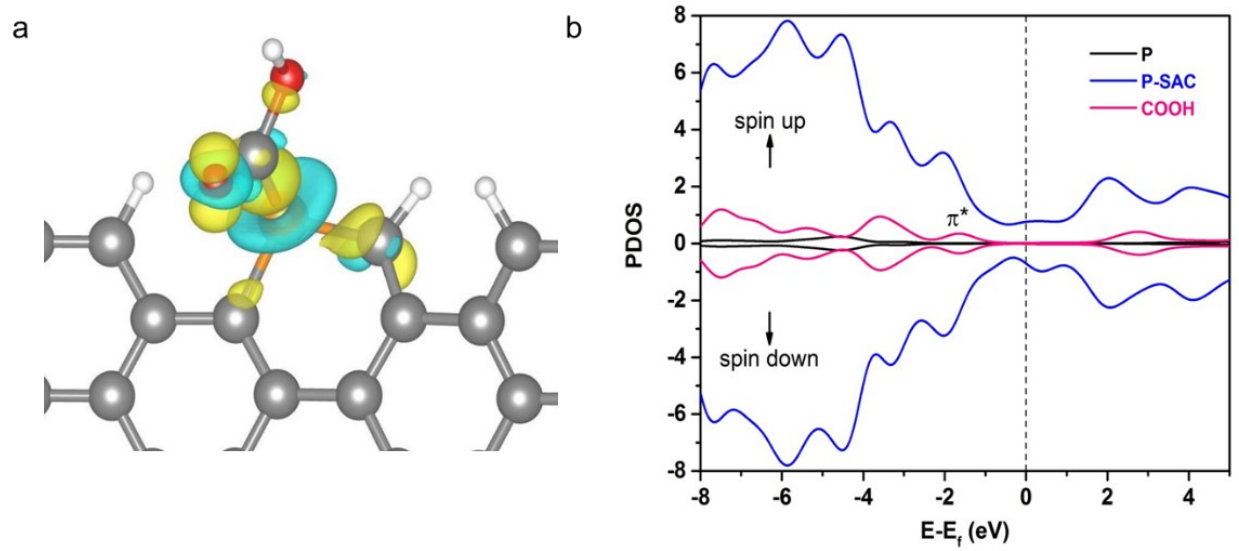

Figure S39. (a) Charge density difference of *COOH intermediate for A1 configuration. For the contour plot, the charge accumulation regions are displayed in yellow while the charge depletion regions are shown in cyan. The contour value of the charge difference density is ±0.02 e/Å^3. (b) Spin-polarized partial density of states (PDOS) projected on P, P-SAC-NG and COOH states in *COOH intermediate for A1 configuration.

Note: The Bader charge of P in A1 is +2.63 |e|, indicating the high oxidation state of P, consistent with the experimental observations. Electron transfers from P-SAC-NG to COOH when forming *COOH intermediate, with the Bader charge of -0.45 |e|, the charge density difference is also shown in fig. S37a. Figure S37b shows the projected density of states (PDOS) of *COOH with A1 configuration, revealing apparent distribution of $\pi^*(CO_2)$ below the Fermi level and strong interaction between P-SAC-NG and $\pi^*(CO_2)$.

Table S1. Specific surface area and pore size distribution of P-SAC-NG and NG.

Samples	BET surface area (m^2/g)	DFDFT method[a]	
		Surface area (m^2/g)	Pore volume (cc/g)
NG	375	381	1.03
P-SAC-NG	1544	1494	2.523

[a]Density Functional Theory method.

Table S2. Chemical contents of P-SAC-NG, NG, degassed P-SAC-NG and NG (obtained from deconvoluted high resolution XPS spectra).

	NG at. %	NG at. % after degassing	P-SAC-NG at. %	P-SAC-NG at. % after degassing
Carbon	89.7	92	85.6	90
Oxygen	4.4	1.8	9.3	4.5
Nitrogen	5.9	6	3.0	3.15
Pyridinic N	1.14 (19.3 %)		0.27 (9.0 %)	
Pyrrolic N	0.99 (16.8 %)		0.28 (22.2 %)	
Graphitic N	3.20 (54.2 %)		1.48 (49.5 %)	
Phosphorus			2.1	

References

1. X. Yang, J. Nash, N. Oliveira, Y. Yan, B. Xu, Understanding the pH Dependence of Underpotential Deposited Hydrogen on Platinum. *Angewandte Chemie International Edition* **58**, 17718-17723 (2019).
2. M. Dunwell *et al.*, Examination of Near-Electrode Concentration Gradients and Kinetic Impacts on the Electrochemical Reduction of CO_2 using Surface-Enhanced Infrared Spectroscopy. *ACS Catalysis* **8**, 3999-4008 (2018).
3. G. Kresse, J. Furthmüller, Efficiency of ab-initio total energy calculations for metals and semiconductors using a plane-wave basis set. *Comput. Mater. Sci.* **6**, 15-50 (1996).
4. G. Kresse, Ab initio molecular dynamics for liquid metals. *J. Non-Cryst. Solids* **192-193**, 222-229 (1995).
5. G. Kresse, J. Hafner, Ab initio molecular-dynamics simulation of the liquid-metal--amorphous-semiconductor transition in germanium. *Phys. Rev. B* **49**, 14251-14269 (1994).
6. P. E. Blöchl, Projector augmented-wave method. *Phys. Rev. B* **50**, 17953-17979 (1994).
7. J. P. Perdew, K. Burke, M. Ernzerhof, Generalized Gradient Approximation Made Simple. *Physical Review Letters* **77**, 3865-3868 (1996).
8. https://janaf.nist.gov/.
9. J. K. Nørskov *et al.*, Origin of the Overpotential for Oxygen Reduction at a Fuel-Cell Cathode. *The Journal of Physical Chemistry B* **108**, 17886-17892 (2004).
10. A. A. Peterson, F. Abild-Pedersen, F. Studt, J. Rossmeisl, J. K. Nørskov, How copper catalyzes the electroreduction of carbon dioxide into hydrocarbon fuels. *Energy & Environmental Science* **3**, 1311-1315 (2010).
11. H. A. Hansen, J. B. Varley, A. A. Peterson, J. K. Nørskov, Understanding Trends in the Electrocatalytic Activity of Metals and Enzymes for CO_2 Reduction to CO. *J Phys Chem Lett.* **4**, 388-392 (2013).
12. G. te Velde *et al.*, Chemistry with ADF. *J. Comput. Chem.* **22**, 931-967 (2001).
13. C. Fonseca Guerra, J. G. Snijders, G. te Velde, E. J. Baerends, Towards an order-N DFT method. *Theor. Chem. Acc.* **99**, 391-403 (1998).
14. E. v. Lenthe, E. J. Baerends, J. G. Snijders, Relativistic regular two-component Hamiltonians. *The Journal of Chemical Physics* **99**, 4597-4610 (1993).
15. W. Tang, E. Sanville, G. Henkelman, A grid-based Bader analysis algorithm without lattice bias. *J. Phys.: Condens. Matter* **21**, 084204 (2009).
16. M. Yu, D. R. Trinkle, Accurate and efficient algorithm for Bader charge integration. *The Journal of Chemical Physics* **134**, 064111 (2011).
17. J. Xu, G. Wu, Z. Wang, X. Zhang, Generation of 2D organic microsheets from protonated melamine derivatives: suppression of the self assembly of a particular dimension by introduction of alkyl chains. *Chem. Sci.* **3**, 3227-3230 (2012).
18. J. Barrio, A. Grafmüller, J. Tzadikov, M. Shalom, Halogen-hydrogen bonds: A general synthetic approach for highly photoactive carbon nitride with tunable properties. *Appl. Catal. B* **237**, 681-688 (2018).